VYSOKÉ UČENÍ TECHNICKÉ V BRNĚ

FAKULTA STROJNÍHO INŽENÝRSTVÍ

ÚSTAV FYZIKÁLNÍHO INŽENÝRSTVÍ

MAGNETOOPTICKÉ ZOBRAZOVÁNÍ A ANALÝZA MIKROSTRUKTUR MAGNETICKÉ DOMÉNY
MAGNETO-OPTICAL IMAGING AND ANALYSIS OF MAGNETIC DOMAIN MICROSTRUCTURES

BAKALÁŘSKÁ PRÁCE
BACHELOR'S THESIS

AUTOR PRÁCE TOMÁŠ MOLNÁR
AUTHOR

VEDOUCÍ PRÁCE M.Sc. JON ANDER ARREGI URIBEETXEBARRIA, Ph.D.
SUPERVISOR

BRNO 2021

Assignment Bachelor's Thesis

Institut:	Institute of Physical Engineering
Student:	**Tomáš Molnár**
Degree programm:	Applied Sciences in Engineering
Branch:	Physical Engineering and Nanotechnology
Supervisor:	**M.Sc. Jon Ander Arregi Uribeetxebarria, Ph.D.**
Academic year:	2020/21

As provided for by the Act No. 111/98 Coll. on higher education institutions and the BUT Study and Examination Regulations, the director of the Institute hereby assigns the following topic of Bachelor's Thesis:

Magneto–optical imaging and analysis of magnetic domain microstructures

Brief Description:

Magneto–optical effects are associated with the interaction of polarized light with magnetized media. Although discovered nearly two centuries ago, magneto–optics is a widely utilized tool for magnetic characterization due to its high sensitivity and versatility. For example, it enables visualization of magnetic domain structures in microscale magnetic systems via wide–field magneto–optical microscopy. The majority of research in this topic has employed linear effects in magnetization to image domains in ferromagnetic materials, where one measures an optical contrast for regions with opposite magnetization orientations. It has been recently shown that even antiferromagnetic materials can be studied using quadratic magneto–optical effects (Voigt effect), making it possible to visualize regions with different spin axis orientation. This work aims to perform a fundamental magneto–optical microscopy study of magnetic thin film and microstructure systems using linear and quadratic effects. Consequently, the microscale magnetization configuration will be interpreted via image processing.

Bachelor's Thesis goals:

1. Literature research of the state–of–the–art on the topic and related methodologies.
2. Imaging of microscopic magnetic domain configurations in magnetic thin films and microstructures using linear and quadratic magneto–optical effects.
3. Developing a platform to determine the space–resolved magnetization vector information from microscopy images.

Recommended bibliography:

BLUNDELL, Stephen. Magnetism in condensed matter. Oxford: Oxford University Press, 2001. Oxford master series in condensed matter physics. ISBN 978-0198505914.

HUBERT, Alex a Rudolf SCHÄFER. Magnetic domains: the analysis of magnetic microstructures. Berlin: Springer, 1998. ISBN 978-3540641087.

XU, Jia, Chao ZHOU, Mengwen JIA, et al. Imaging antiferromagnetic domains in nickel oxide thin films by optical birefringence effect. Physical Review B. 2019, 100(13). ISSN 2469-9950. Dostupné z: doi:10.1103/PhysRevB.100.134413

Deadline for submission Bachelor's Thesis is given by the Schedule of the Academic year 2020/21

In Brno,

L. S.

prof. RNDr. Tomáš Šikola, CSc.	doc. Ing. Jaroslav Katolický, Ph.D.
Director of the Institute	FME dean

Abstrakt

Magnetooptické jevy popisují interakci polarizovaného světla s magnetizovaným médiem. I když byla objevena téměř před dvěma staletími, díky své vysoké citlivosti a všestrannosti je magnetooptika široce využívaným nástrojem pro magnetickou charakterizaci. Například umožňuje vizualizaci doménové struktury v magnetických strukturách pomocí širokoúhlého magnetooptického mikroskopu. Většina výzkumných prací v této oblasti využívá jevů lineárních v magnetizaci k zobrazování domén ve feromagnetických materiálech, kde se měří optický kontrast pro oblasti s opačnou orientací magnetizace. Nedávno bylo prokázáno, že i antiferomagnetické materiály lze studovat pomocí kvadratických magnetooptických jevů (Voigtův jev), což umožňuje vizualizovat oblasti s různou orientací spinové osy. V této práci jsme provedli základní studii magnetických tenkých vrstev a mikrostruktur pomocí magnetooptické mikroskopie s využitím lineárních a kvadratických efektů. Současně byly interpretovány konfigurace magnetizace spojitých a strukturovaných magnetických tenkých vrstev v mikroskopickém měřítku s využitím metod zpracovávání obrazu vyvinutých v této práci, vedoucím ke kvantitativní vektorové magnetometrii. Nakonec, byla provedena studie koexistence feromagnetických a antiferomagnetických fázových domén v FeRh užitím magnetooptické mikroskopie.

Summary

Magneto-optical effects are associated with the interaction of polarized light with magnetized media. Although discovered nearly two centuries ago, magneto-optics is a widely utilized tool for magnetic characterization due to its high sensitivity and versatility. For example, it enables visualization of magnetic domain structures in microscale magnetic systems via wide-field magneto-optical microscopy. The majority of research on this topic has employed linear effects in magnetization to image domains in ferromagnetic materials, where one measures an optical contrast for regions with opposite magnetization orientations. It has been recently shown that even antiferromagnetic materials can be studied using quadratic magneto-optical effects (Voigt effect), making it possible to visualize regions with different spin axis orientations. In this work, we perform a fundamental magneto-optical microscopy study of magnetic thin film and microstructure systems using linear and quadratic effects. Consequently, the microscale magnetization configuration of continuous and patterned magnetic thin films is interpreted via the image processing strategy developed in this thesis, leading to quantitative vector magnetometry. Moreover, the coexistence of the ferro- and antiferromagnetic phase domains in FeRh films was investigated using optical and magneto-optical microscopy.

Klíčová slova

vektorová magnetometrie, magnetické domény, magnetooptika, Kerrův jev, Voigtův jev, FeRh, permalloy, fázová přeměna

Keywords

vectorial magnetometry, magnetic domains, magneto-optics, Kerr effect, Voigt effect, FeRh, permalloy, phase transition

Prohlašuji, že jsem diplomovou práci *Magnetooptické zobrazování a analýza mikrostruktur magnetické domény* vypracoval samostatně pod vedením M.Sc. Jona Andera Arregiho, Ph. D., s použitím materiálů uvedených v seznamu literatury.

Tomáš Molnár

Tomáš Molnár

Contents

Introduction

Magnetism may be considered one of the foundation stones of large group of modern technologies. Magnetic materials are applied in a wide pallet of applications, from magnetic recording as a method for information storage, to magnetic levitation and biomedicine. We can say undoubtedly that in the last decades, magnetic recording represents the most quickly expanding application area of magnetic materials, together with energy conversion (i.e., power transformers), sensors, and more. For example, technological advances in the field of nanomagnetism permitted to sustain the exponential growth of density of information (bits per unit area) in hard disk drive devices, ever since their appearance in the 1950s. Here, the recording medium - a magnetic layer where a unique magnetic pattern is written in terms of regions magnetized in different directions - is read by a nearby standing writing head composed of a magnetic sensor as it moves past. After obtaining information, the reading head leaves the magnetic pattern unaffected.

Nevertheless, the maximum storage density that can be reached via this strategy has a limit. At some point, the memory particles or cells become too small to withstand the stochastic reorientation of bits by thermal fluctuations, which is the so-called superparamagnetic limit [1]. On the other hand, in 2017, it was shown that it is possible to fabricate a single-atom bit, which opens the door to atomic-scale data storage [2]. In addition, a large technological potential relies on combining magnetic materials with semiconductors, i.e., magnetic semiconductors. Devices based on this material platform could benefit from semiconductors' logic operation and magnetic materials' memory functionality [3]. Most studies involving these materials use alloy semiconductors, which include magnetic particles implemented to the semiconductor. Similar devices utilize electron's charge as well as the spin. Such devices are known as spintronic devices, which are the objects of study in the scientific field of spintronics [3, 4]. Spintronics is becoming one of the most promising next-generation technologies. These devices envision operation at lower power consumption, as well as could enhance data processing speed and memory.

Starting from the 19th century, scientists began to realize the concept of elementary magnets constituting the magnetic matter similarly as matter consists of atoms and molecules. This concept explained the magnetic saturation phenomenon, which means that all elementary magnets are oriented alike, as well as why it is impossible to separate a magnet into the south and north pole. In order to describe the magnetic behavior better, Langevin [5] used the approach of statistical thermodynamics and already developed a theory of paramagnetism in 1905. Langevin found that independent molecular magnets at room temperature only have a weak magnetic response, so he suggested that elementary magnets must possess a strong magnetic interaction. Shortly after his theory was published, Weiss introduced a concept of a "molecular field" acting between molecular magnets and promoting their parallel alignment [6]. Upon this, he was able to explain the saturation magnetization dependence on temperature. Formally, the magnitude of the molecular field Weiss hypothesized was extremely large. Only with the arrival of quantum mechanics, Heisenberg recognized the origin of such a virtually large field and explained the interaction as a quantum-mechanical exchange effect (or interaction) [7].

Weiss also pointed out the possibility that the different parts of the crystal may possess different magnetization orientation. Later, these regions within which magnetization is uniform were termed as magnetic domains [8]. For a long time, there were just indirect proofs of the existence of magnetic domains. One of the simplest magnetic domain-imaging methods, but

still very frequently used nowadays, is the Bitter method [9]. Colloidal magnetite particles (or magnetite powder) are applied to the surface of a sample. The magnetic field generated by individual domains acts on the magnetic particles, making them segregate on the domain boundaries. Nowadays, there is a huge variety of techniques for imaging magnetic domains, among which most prominent are: electron microscopy (e.g., Lorentz microscopy, scanning electron microscopy with polarization analysis), scanning probe microscopies, x-ray magnetic microscopies, and last but not least, magneto-optical microscopy. Magneto-optics is the field that studies the interaction of light with magnetized matter. Despite its resolution limit being a limiting factor for nanoscale science (compared to electron microscopy or magnetic force microscopy), it is a very versatile and non-destructive technique capable of direct observation of magnetic domains. Furthermore, it was shown recently that also antiferromagnetic domains can be imaged using magneto-optics [10]. So far, antiferromagnetic domains in metallic thin film systems could not be observed, mainly because antiferromagnetic ordering is very sensitive to defects and crystallographic faults (which are common in metallic thin film), such that antiferromagnetic domain sizes are usually in the < 500 nm range.

An entirely new technology emerging from antiferromagnetic spintronics promises a huge impact on the view of modern electronics [11]. Current data storage utilizing magnetic memory by using ferromagnets takes advantage of easy writing and reading of information in ferromagnetic storage since ferromagnets are affected by magnetic fields. In comparison, the antiferromagnets are inert to external magnetic fields, making this technology more reliable since it enhances its robustness [12]. Furthermore, they do not create any magnetostatic (or dipolar) field; because of this, the individual memory cells can be packed closer to each other, which results in higher information storage densities. Predictions also suggest higher energy efficiency and 100 - 1000 times faster switching speed limit than conventional ferromagnets [11].

In this thesis, magnetic domain observation via magneto-optical microscopy has been investigated. Firstly, the theoretical considerations of magnetic materials (Chapter 1) and magneto-optical effects (Chapter 2) have been summarized. Then, a computational platform for visualizing of the in-plane magnetization vector was developed and applied on results measured by first-order magneto-optical effects (Chapter 3). In the end, second-order magneto-optical effects measurements were performed to imaging ferromagnetic as well as antiferromagnetic samples (Chapter 4).

1. NANOMAGNETISM

The field of nanomagnetism is dedicated to the study of nanoscale magnetic objects, such as thin films, nanostructures, and nanoparticles. It generally deals with the following scientific questions: What role does magnetism play at the nanoscale? What are the emergent phenomena upon reducing the size?

Once we get to submicron dimensions ($1 \, \text{nm} - 1 \, \mu\text{m}$), we encounter specific magnetic phenomena. This length range becomes relevant because the most prominent magnetic interactions possess a characteristic interaction range at the nanoscale, from short-range exchange interactions ($0.1 - 1 \, \text{nm}$) to long-range interactions such as magnetostatic effects ($10 - 100$ nm and above) [13].

1.1. Magnetization and magnetic materials

Imagine a magnetic field in free space. We can describe such a magnetic field by the $\boldsymbol{B}$-field (or magnetic induction) and the $\boldsymbol{H}$-field (or magnetic field strength), which are proportional to each other via the permeability of free space $\mu_0 = 4\pi \cdot 10^{-7}$ H/m

$$\boldsymbol{B} = \mu_0 \boldsymbol{H}. \tag{1.1}$$

If we consider a magnetic solid in the free space, the two magnetic field vectors are no longer linear. The most general relationship now reads as

$$\boldsymbol{B} = \mu_0 (\boldsymbol{H} + \boldsymbol{M}), \tag{1.2}$$

where $\boldsymbol{M}$ is the magnetization of the solid defined as a total magnetic moment per unit volume,

$$\boldsymbol{M} = \frac{\sum_i \boldsymbol{\mu}_i}{V}. \tag{1.3}$$

Magnetization is a material characteristic. It depends on the magnetic dipole moments of the ions, atoms, and molecules contained in the material and the interactions between them [14]. Furthemore, these interactions are often dependent on external conditions such as temperature, pressure, etc.

The magnetic induction $\boldsymbol{B}$ may be thought of as the flux density inside the material. Generally speaking, the magnetic flux density inside the material is different from the outside. By comparing the balance between the internal and external flux densities, magnetic materials are classified into different classes [15]:

- Internal flux being less than outside: we call such materials diamagnetic. Diamagnetic materials have no overall magnetic moment (i.e., they possess zero magnetization). The reaction of diamagnetic materials on an applied field is creating magnetization opposite to the field direction. Diamagnetism is a relatively weak effect and, in fact, occurs in all materials [15].

- Internal flux being a bit larger than outside: this class of materials also possesses a zero net magnetization. However, the internal flux is slightly larger than outside. These

may be either paramagnetic or antiferromagnetic materials. In both materials, individual atoms possess a magnetic moment. In the case of paramagnetic material, they are randomly oriented, so they average out to zero (see Figure 1.1a).In contrast, adjacent magnetic moments in an antiferromagnet are oriented antiparallel to each other, so the total magnetic moment cancels out (see Figure 1.1b). Applying a magnetic field (which needs to be very large in the case of an antiferromagnet) causes the magnetic moments to partially line up with the field, so that the material develops a small net magnetization.

- Internal flux being much larger than outside: such materials are either ferromagnets or ferrimagnets. The magnetic moments in a ferromagnet tend to lie parallel to each other and can be quite easily manipulated by an external field (see Figure 1.1c)). On the other hand, ferrimagnets are similar to antiferromagnets in that they are composed by two sublattices with opposing magnetic moment orientations, except in that the magnetic moments one of the sublattices are larger than in the other, so the net magnetic moment is non-zero (see Figure 1.1d)).

The magnetic moments' arrangement schematic of materials discussed above are shown in Figure 1.1.
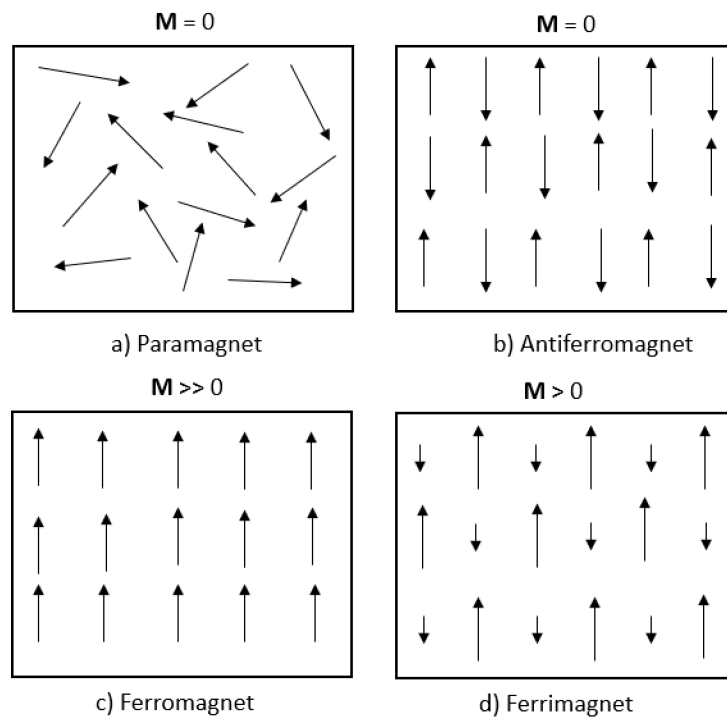
Figure 1.1.: Schematic of the ordering of magnetic dipole moments in a typical a) paramagnet, b) antiferromagnet, c) ferromagnet, d) ferrimagnet

However, so far we treated the magnetic materials just in terms of the flux density or magnetization, but this is not the only measure to characterize them. Another material property is called magnetic susceptibility χ_m and is defined as the ratio of M to applied field H. In other words, the susceptibility tells us how a materials' magnetization reacts to H-field. In the simplest case, i.e., linear, isotropic, and homogeneous material takes the form [14]

$$M = \chi_m H. \tag{1.4}$$

A similar property, comparing B-field to H-field, is known as magnetic permeability μ_m. And again, in the simple case, the permeability is given by

$$B = \mu_m H. \tag{1.5}$$

Combining this expressions with Equation 1.2, we get a relation between the two material characteristics

$$\mu_m = \mu_0(1 + \chi_m). \tag{1.6}$$

Previously, we classified magnetic materials according to the magnetic flux density. It is also possible to do so by χ_m (or μ_m). This classification can be nicely seen in the so-called magnetization curves, M (or B) vs H graphs [15]. A few exemplary magnetization curves of the already mentioned materials, which are also the most common in nature, are plotted schematically in the Figure 1.2.
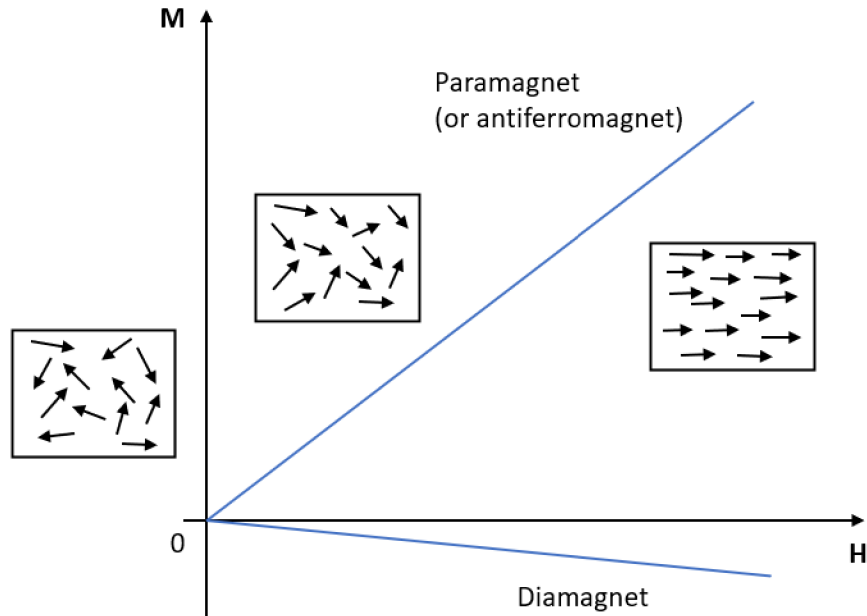
Figure 1.2.: Magnetization curves (M vs H curves) of paramagnetic (or antiferromagnetic) and diamagnetic materials. The magnetization curve of the paramagnet is supported by schematics indicating the influence of the externaly applied magnetic field H on magnetic moments orientation.

As represented in Figure 1.2, we can see that the magnetization curves for diamagnetic, paramagnetic (and even antiferromagnetic) materials are linear in H, and generally very large fields need to be applied to cause a noticeable change in magnetization. Another important note is that if we remove the external field, the magnetization goes to zero. In the case of diamagnets, the slope, i.e., χ_m, is negative, which corresponds to the action of magnetizing the material against the externally applied H-field. χ_m is also slightly lower than 1, meaning that diamagnetism is a weak effect. In general, paramagnets' and antiferromagnets' susceptibility is positive and larger than 1 [14]. For ferromagnets (not shown in Figure 1.2), both χ_m and μ_m have tensorial form, implying that the M vs H relation is highly nonlinear (and a multiple--valued function). This aspect will be discussed in the following sections.

1.2. Magnetic interactions and domain configurations

An approach to describe a material's magnetic properties consists of considering the energy terms arising from the different interactions in the system. In the thesis, we will mainly focus on ferromagnetic materials with a nonzero net magnetization, while covering some aspects of antiferromagnetic materials. The most fundamental interactions are

- interactions between the magnetic moments within the material,

- the effect of an externally applied magnetic field (or additional external factors), and

- the material's crystallographic structure.

All these interactions contribute to the total energy of the system. Due to the competition of the different interactions the system's magnetic moment configuration and net magnetization vector M are chosen so that the total free energy finds either an absolute or relative minimum (stable or metastable states). This condition also tells us that the torque on all magnetic moments in the system has to disappear. A quantitative approach to the problem is often based on calculating the torque conditions, which result in the so-called micromagnetic equations. This energy minimalization principle leads to the formation of non-uniform magnetization states or magnetic domains.

1.2.1. Magnetic domains

Ferromagnetic domains are areas in a ferromagnet inside which neighboring magnetic moments are parallel to each other. There are many different domain structures and textures. The very basic classification is whether the magnetization is uniform over the whole body (single-domain state) or the magnetization splits into many domains (multi-domain state).

Large, bulk-like ferromagnetic materials prefer being in a multi-domain state; however, if we scale down the dimensions and reach the so-called critical size, no spatial-dependent magnetic structure appears [16], and the ferromagnet is in the single-domain state (e.g., ferromagnetic nanostructures and nanoparticles in the $\sim$100 nm length scale). For patterned thin film structures with intermediate length scales (approximately 1 - 100 μm), characteristic domain states often consist of a magnetic flux-closure patterns, in which the magnetization forms a closed loop. One example is Landau's flux-closed domain pattern, or Landau structure, in which the closure is achieved by breaking the magnetic structure into the multi-domain state. Another interesting example is the magnetic vortex, where the magnetization whirls in micrometer size disks, choosing to continuously circulate around the disc azimuth rather than creating multiple domains. Both states are shown in Figure 1.3a), the figure is accompanied by a radial color-wheel indicating magnetization orientation. In addition, thin film and multilayer systems with out-of-plane or perpendicular anisotropy also show maze-like or labyrinthic domains known as magnetic stripe domains (see Figure 1.3b)).

Magnetic structures analogous to ferromagnetic domains also appear in antiferromagnets, i.e., antiferromagnetic domains. Here, we cannot talk about a particular magnetic moment orientation, as every region of the system contains opposed moments that cancel each out. However, we can define the spin axis orientation of a region (also known as Néel vector) [17]. We may imagine splitting the body of the antiferromagnet in several regions, each having its own spin-axis orientation (see Figure 1.4). Direct observation of the antiferromagnetic domains is more challenging than for ferromagnets, because of no net magnetization, which is why they

are little known [18]. Furthermore, very high external magnetic fields are usually needed in order to manipulate their magnetic moments

On the following the most important magnetic interactions in ferromagnetic (and antiferromagnetic) materials are listed, with a special focus on the kind of magnetic domain configurations they promote or facilitate.
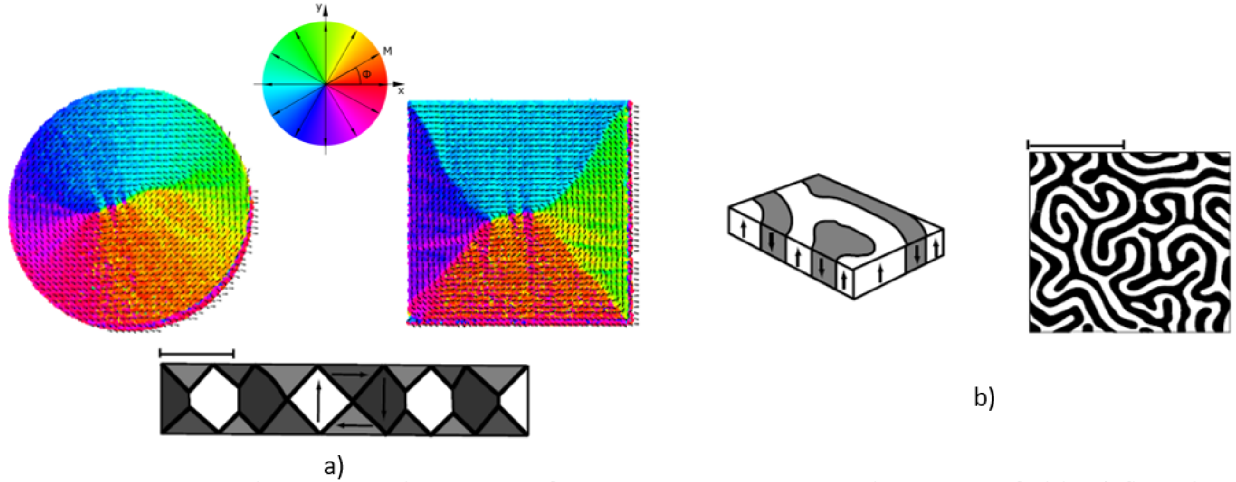
Figure 1.3.: Typical magnetic domain configuration in zero external magnetic field - a) flux closure patterns in thin film magnetic materials (i.e. magnetic vortex, Landau pattern). Colorized images consist of experimental data that are the result of the quantitative magnetometry platform developed in this thesis. The figure includes a radial color-wheel indicating the orientation of magnetization; b) stripe domains in magnetic thin films and multilayers with perpendicular magnetic anisotropy. Gray-scale images were taken from [19].
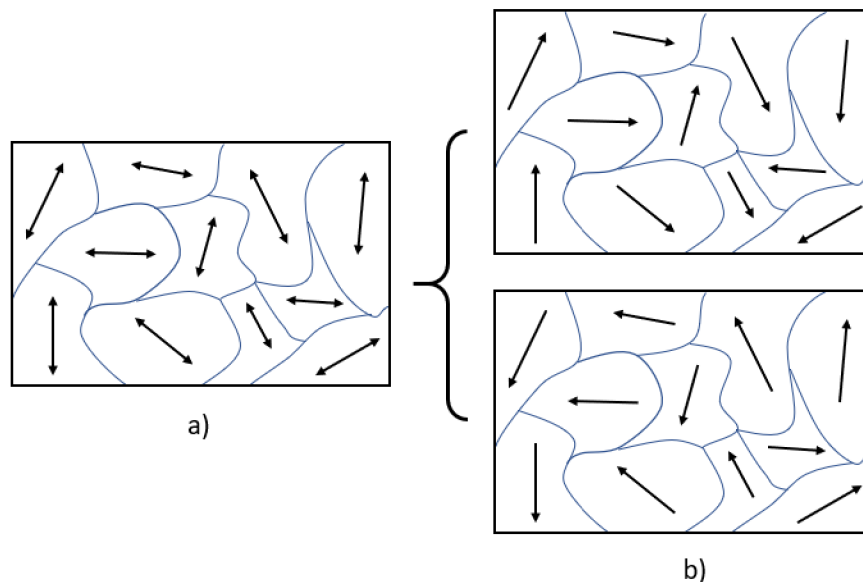
Figure 1.4.: a) Antiferromagnetic domain microstructure schematic with Néel vectors indicated in each domain; b) subdivision of the microstructure to domains within which the net magnetization is non-zero.

1.2.2. Exchange energy

Consider a ferromagnet in an applied magnetic field $\boldsymbol{B}_{ext}$; the Hamiltonian to solve in this case has a form [14]

$$\hat{\boldsymbol{H}} = -\sum_{ij} J_{ij}\boldsymbol{S}_i \cdot \boldsymbol{S}_j + g\mu_B \sum_i \boldsymbol{S}_i \cdot \boldsymbol{B}_{ext}, \tag{1.7}$$

where $\boldsymbol{S}$ is an electron spin, indices i and j refer to all spins in a ferromagnet, constant J_{ij} is the exchange constant, g is the gyromagnetic ratio, and μ_B is the Bohr magneton. The first term is called the Heisenberg exchange energy and represents an interaction favoring the parallel or antiparallel alignment of adjacent spins, depending on whether $J_{ij} > 0$ (ferromagnet) or $J_{ij} < 0$ (antiferromagnet), respectively. The second term is called the Zeeman energy and causes spins to line up with the applied field.

The magnetic exchange interaction is a fully quantum mechanical interaction, which originates from the electrostatic repulsion felt by electrons and Pauli's exclusion principle. Its treatment was firstly introduced by Heisenberg in 1928, thus establishing the physical origin of (anti-) ferromagnetic order in materials.

In order to describe a very wide of phenomena in nanomagnetism, it is often sufficient adopting a micromagnetic description, in which, we can describe the magnetization of the system as $\boldsymbol{m}(\boldsymbol{r}) = \boldsymbol{M}(\boldsymbol{r})/M_s$ in the continuum approximation. The atomic structure is averaged out, so we take $\boldsymbol{m}(\boldsymbol{r})$ as a smoothly varying function with constant amplitude (differing only in direction).

Imagine a ferromagnet with all magnetic moments pointing "up," i.e., the lowest entropy state or ground state. If we let the system evolve in time, we will see that the system will increase entropy and break the ideally ordered ground state's symmetry [14]. After falling into such an energetically favorable state, our efforts to change it will lead to resistance. As a classical analogy, we can imagine cubic crystal with lattice parameter a. If we displace a plane of bonds by x, we will induce a strain $e = x/a$, which will cause a stress $\sigma = Ge$, where G is an elastic modulus. A force acting on one bond is then $F = \sigma a^2 = Gxa$, energy stored in the bond is $\frac{1}{2}Gax^2$. We can write that $\langle x^2 \rangle \sim 1/G$, which we can interpret as follows: the finite character of the elastic modulus is related to finite displacement fluctuations [14]. Crystals have elastic energy stored in bonds proportional to $(\nabla x)^2$. A similar concept can be used for ferromagnets, where the order parameter is a magnetization $\boldsymbol{m}$. From the first term in Hamiltonian (1.7), we saw that spins tend to align electron spins, which causes their magnetic dipole moments to align. We must provide extra energy, proportional to $(\nabla \boldsymbol{m})^2$, to misalign the spins with respect to each other. After taking advantage of the similarity, the energy term can be expressed as [16]

$$E_{ex} = A \int (\nabla \boldsymbol{m})^2 dV, \tag{1.8}$$

where the parameter A is a material constant termed as the exchange stiffness, an approximate relation to the atomic scale exchange parameter is [19]

$$A \approx JS^2 Z_c/a, \tag{1.9}$$

where J is the exchange constant, S is the electron's spin, and Z_c is the number of atoms

per unit cell. The exchange energy is responsible for the existence of ferromagnetic and antiferromagnetic order in magnetic materials, and in turn, of the establishment of long-range magnetic order.

For the exchange energy to be the lowest, it is most beneficial to have single domain states or as least domains as possible. The occurrence of domain walls (regions with spatially rapidly varying moment orientation) is then very energetically costly [15] because the magnetization has to transition from one domain orientation to the other. One way of minimizing this additional energy cost is to get rid of the domain wall and make the magnetization vary smoothly; an instance might be vortex domains. The opposite also works in some cases, and that is to form very narrow domain walls. On the other hand, the domain walls occur in order to minimize the free energy of a whole system at the expense of the gain in exchange energy, finding a compromise by minimizing other magnetic energy contributions.

1.2.3. Magnetocrystalline anisotropy

A material possesses a property of having an easy and hard axis. The easy axis denotes energetically advantageous magnetization orientation, whereas a hard axis refers to the most energetically costly orientation. The magnetocrystalline anisotropy energy term is regularly defined as a difference between energies corresponding to magnetization lying along the easy and hard axis. The overall anisotropy energy comprises an intrinsic and induced anisotropy. Intrinsic anisotropy is a consequence of a crystal structure, and some authors claim that also of the shape [15] others prefer classifying the material's shape to magnetostatic energy [16]. Whereas induced anisotropy can be achieved by proper sample preparation method, it results from deviations from an ideal crystal structure.

The magnetocrystalline anisotropy is of intrinsic origin; the symmetry of the lattice directly influences anisotropy energy. As a result, the energy can be written as a series of expansion of direction cosines, taking into account the angle between the magnetization and the easy axis [16].

For instance, a cubic structure (e.g. Fe, FeRh) the anisotropy energy density term can be expressed as

$$E_{anis,c} = K_{c1}(m_1^2 m_2^2 + m_2^2 m_3^2 + m_1^2 m_3^2) + K_{c2} m_1^2 m_2^2 m_3^2, \qquad (1.10)$$

where K_1 and K_2 are material constants, termed as the anisotropy constants, and m_i are projections of magnetization into easy orientations. A material having this kind of symmetry is said to have fourfold anisotropy. These materials have two orthogonal easy axes, as well as two orthogonal hard axes. In iron, the easy axes are cube edges $\langle 100 \rangle$, and the hard axes are cube diagonals $\langle 111 \rangle$ [15].

Some materials may possess a so-called uniaxial anisotropy (i.e. Co); this is a case for hexagonal materials. The easy axis lies along the hexagonal axis [0001], and so the energy can be written as

$$E_{anis,u} = K_{u1} \sin^2 \phi + K_{u2} \sin^4 \phi, \qquad (1.11)$$

where ϕ is the angle between the easy axis and the magnetization.

Magnetocrystalline anisotropy promotes the formation of domains with the magnetization direction along the easy axes. If no external magnetic field is applied, the magnetization stays or tilts towards the easy directions; hence, observing such a state helps us find the sample's easy axes.

As the magnetization changes from one domain to the other, it will lie along the hard axis at some point. This magnetization orientation brings a high energy penalty; thus, domain walls are also unfavorable. To reduce the energy cost, narrower domain walls are preferable in high magnetocrystalline anisotropy materials (i.e., hard magnetic materials).

1.2.4. Zeeman energy

The Zeeman energy describes the interaction of magnetization with an external magnetic field, in accordance with the second Hamiltonian term in the Equation (1.7). In the continuum approximation, we write

$$E_Z = -M_S \int \boldsymbol{H}_{ext} \cdot \boldsymbol{m} dV,$$ (1.12)

where $\boldsymbol{H}_{ext}$ is the external magnetic field. The favorable domain configurations with Zeeman energy's are those with their magnetic moments pointing along the external field [16].

1.2.5. Magnetostatic energy

The magnetostatic energy term represents the interaction arising from long-range magnetic dipole-dipole interactions, i.e., the interaction of a magnetic moment in the ferromagnet body with the rest of magnetic moments in the system. Sometimes called the stray field energy, it comes from the Maxwell equation term for $\nabla \cdot \boldsymbol{B} = 0$, which for a magnetic body states (from Equation (1.2)): $\nabla \cdot \boldsymbol{H}_d = -\nabla \cdot \boldsymbol{M}$. Here $\boldsymbol{H}_d$ is named as the demagnetizing field and it represents a divergent magnetic field at the surface or extremes of a magnetized body, created as a result of the divergence of magnetization at these extremes, which is suddenly interrupted [14]. We can imagine this situation by assuming "magnetic charges" or virtual magnetic monopoles. These charges act as sources and sinks of the demagnetizing field. They always appear in couples to fulfill the condition of $\nabla \cdot \boldsymbol{B} = 0$. If the magnetization was to point out of the magnetic body and create a magnetization source, magnetic charges would appear and act against the magnetization to create magnetic flux closure patterns in the optimal case. The stray field energy is thus one of the main reasons why magnetic domains occur.

Quantitatively the energy can be expressed as follows [16]:

$$E_{demag} = -\frac{1}{2} \int \boldsymbol{H}_d \cdot \boldsymbol{M} dV,$$ (1.13)

where we integrate over the sample volume. The stray field originates from the magnetization, and it can be related to it by the following linear relation [15]

$$\boldsymbol{H}_d = -\hat{\boldsymbol{N}} \boldsymbol{M},$$ (1.14)

where $\hat{\boldsymbol{N}}$ is the demagnetizing tensor, a quantity that purely depends on the shape of the ferromagnetic body. In the particular case of an ellipsoidal magnet, the demagnetizing tensor can

be diagonalized in a proper reference frame, such that it can be represented by demagnetizing factors, fulfilling the condition $Tr(\hat{N}) = N_x + N_y + N_z = 1$. Some special cases may be deduced, for instance, a sphere $N_x = N_y = N_z = 1/3$, or a thin $xy-$plane film $N_x = N_y = 0$, $N_z = 1$.

Let us illustrate the whole concept for the case of a thin film; see Figure 1.5. When the magnetization is oriented in the plane of the film, no magnetic charges appear at the horizontal ends of the film because they are very distant from each other. For this sake, no demagnetizing field will play a role. On the other hand, if we orient the magnetization out of the film plane, the magnetic charges created at the areas where magnetization ends suddenly generate a strong demagnetizing field acting against the magnetization direction. Hence it is less energetically costly to orient the magnetization in the plane of a thin film [20].
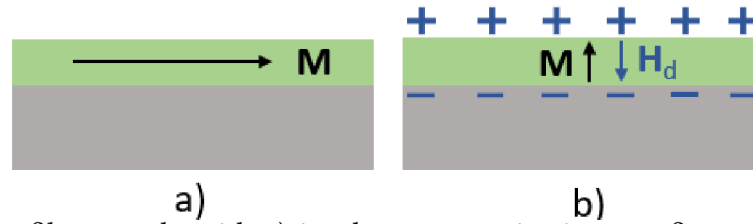

Figure 1.5.: A thin film sample with a) in-plane magnetization, configuration which creates no magnetic charges and is energetically favorable in terms of the magnetostatic energy; b) out of plane magnetization configuration resulting in appearance of magnetic charges generating demagnetization field acting against the magnetization.

This concept applies well in the "thicker" samples, i.e., 20 - 30 atomic levels [15]. However, if we go down in thickness, surface will be more significant than the volume. Moreover, the surface may be thought of as a defect due to the absence of the neighboring atoms, which gives rise to an effect called surface anisotropy. The surface anisotropy, together with the exchange interaction, forces the magnetic moments to be oriented perpendicular to the surface.

We may notice that the equation describing the magnetostatic energy term is similar to the Zeeman energy term in Equation (1.12), which reflects the fact that it can be understood as a "self-acting field". Moreover, substituting the Equation (1.14) to the magnetostatic energy term, leads to the following expression:

$$E_{shape} = \frac{1}{2}(N_x M_x^2 + N_y M_y^2 + N_z M_z^2). \tag{1.15}$$

Which, again, looks like another already-discussed energy term - the magnetocrystalline energy term. This expression may be considered a shape anisotropy term, which again suggests preferential magnetization directions due to the shape of the ferromagnet. The shape anisotropy is an important energy term not only in thin films but also in high aspect ratio nanostructures and nanoparticles.

Typical stray field-free domains are flux-closure patterns [16], which minimize the volume of application of this self-acting field in space and thus reduce their magnitude. If the magnetization flux closes and no stray field is leaked outside the ferromagnetic body, no magnetic charges appear, and the demagnetizing energy contribution can be largely reduced.

1.2.6. Magnetostriction and magnetoelastic energy

When a ferromagnet is exposed to a magnetic field, it experiences a very slight change in its dimensions, termed as magnetostriction, as a result of the coupling between magnetic and mechanical effects [15]. For most materials, this effect is minimal. However, it can often play a large role in domain formation. For instance, in iron, adjacent domains with perpendicular magnetization will try to elongate along magnetization axes. Both cannot stretch simultaneously; this introduces elastic strain energy. If we want to describe these effects quantitatively , we need to define a tensor of elastic distortion, which considers a new degree of freedom [16].

For the materials and phenomena investigated in this thesis, magnetostriction and magnetoelastic effects are in principle negligible unless otherwise stated.

1.3. Hysteresis and magnetization processes

In the case of ferro- and ferrimagnetic materials, the M vs H curves usually displays a non-linear and irreversible behavior to the applied field. These curves called hysteresis loops and are obtained by applying a cycling H-field on the system in order to reverse the direction of magnetization, while at the same time recording the projection of M along the field axis. On the following, the principal properties of magnetic hysteresis and the domain processes are described.

1.3.1. Ferromagnetic hysteresis

In contrast with the M vs H curves in Figure 1.2, the magnetization curve of ferromagnet or ferrimagnet is plotted in the Figure 1.6. A fact worth mentioning is that the two figures showing magnetization curves have entirely different scales. We may also deduce that the χ_m is positive, far greater than 1, and generally a complex function of the applied field H. Increasing the applied field magnitude will increase the material's magnetization, but at some point, the magnetization stops growing. The reached value is known as the saturation magnetization M_s, and it corresponds to a state in which all magnetic moments are pointing in the applied field direction. Reducing the H-field to zero generaly does not cause magnetization to drop to zero. This state is called a remanent magnetization M_r and is the reason why ferromagnets are frequently termed as the "permanent magnets". A key characteristic of ferro- and ferrimagnetic materials is that the projected magnetization M only becomes zero after the application of a negative field (-H_c), defined as the coercive field. The corresponding process is seen if we vary the field in the opposite direction, such that $M(H) = -M(H)$. Large variations of M with small H changes (where the slope of the loop gets large) are usually a signature of several domain processes, such as the nucleation and expansion of domains with reversed orientation Additional characteristics of domain processes within the hysteresis loops are discussed below.

1.3.2. Domain walls in thin films

The orientations of magnetization in neighboring magnetic domains differ; thus, there has to be a certain boundary between them. This boundary is called a domain wall. The existence of domains directly indicates the existence of domain walls. We can classify them according to the angle between the magnetization in the two domains. A 180° domain wall occurs between domains with opposite magnetization, whereas a 90° domain wall separates two domains having
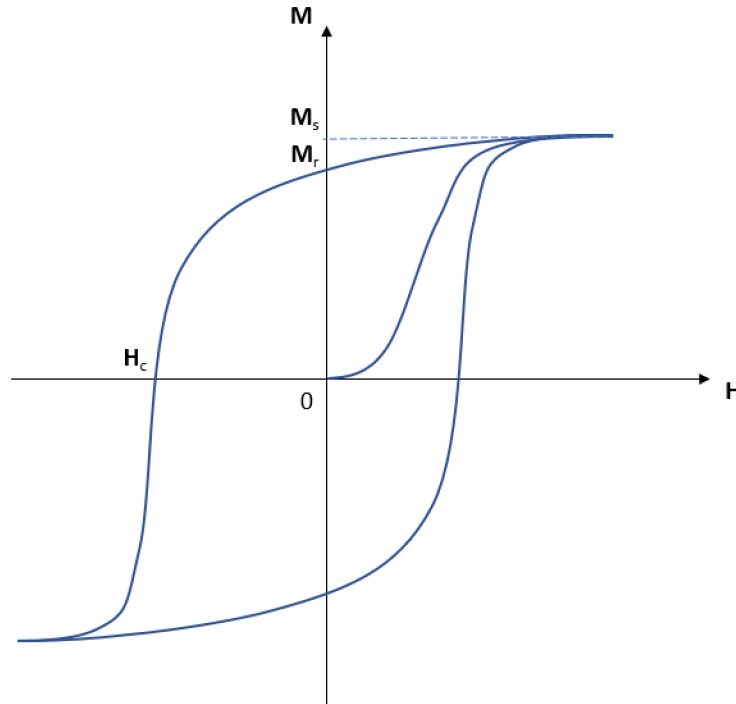
Figure 1.6.: A ferromagnetic hysteresis loop graph including parameters defining the material: H_c - coercive field, M_s - saturation magnetization, and M_r - remanent magnetization. The graph is supported with initial magnetization curve.

perpendicular magnetization. A typical thickness of a domain wall is $\sim$10 nm to 10 µm [15]; the width is again a consequence of a balance between energy competition. The magnetization has to rotate across a domain wall from one orientation to the other, bringing a high energy cost. The most favorable is to create domain walls that do not introduce any demagnetizing fields [15].

One of the most common types of 180° walls is a Bloch wall. In the Bloch wall, the magnetization rotates in a plane parallel to the boundary plane of the wall. Another type is a Néel wall, in which the magnetization rotates in a plane perpendicular to the wall's plane. Even though a Bloch wall is usually less energetically costly, Néel walls are more typical in thin films because the virtual magnetic charges are created on the wall's surface rather than on the film surface, thus avoiding out-of-plane moment configurations, and leading to a reduction in magnetostatic energy. For the Néel wall to be stable, the film must be thinner than the wall's width [19]. Both types of domain walls are displayed in the Figure 1.7.

1.3.3. Magnetization processes

Figure 1.8 shows the schematic of a part of the magnetization curve. Initially, at zero field , the sample is in a demagnetized state, and all domains' magnetizations completely cancel out. Next, an external field is applied in the horizontal direction, slightly off the sample's easy axis. Different processes occur when applying an external field on a demagnetized ferromagnet. The first process to happen consists of domain wall motion: domains with magnetization orientation closest to the applied field orientation start growing, whereas domains with opposite
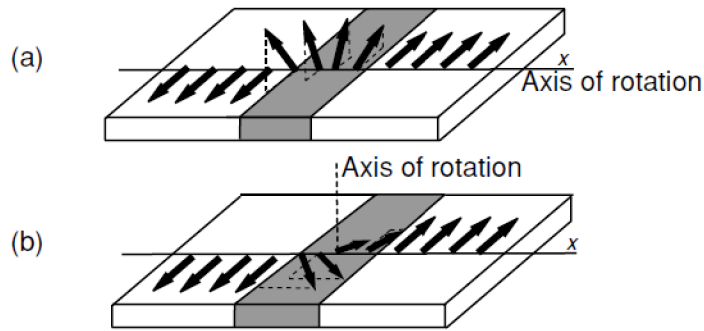
Figure 1.7.: Schematic of magnetic domain walls: a) Bloch wall, b) Néel wall, taken from [19].
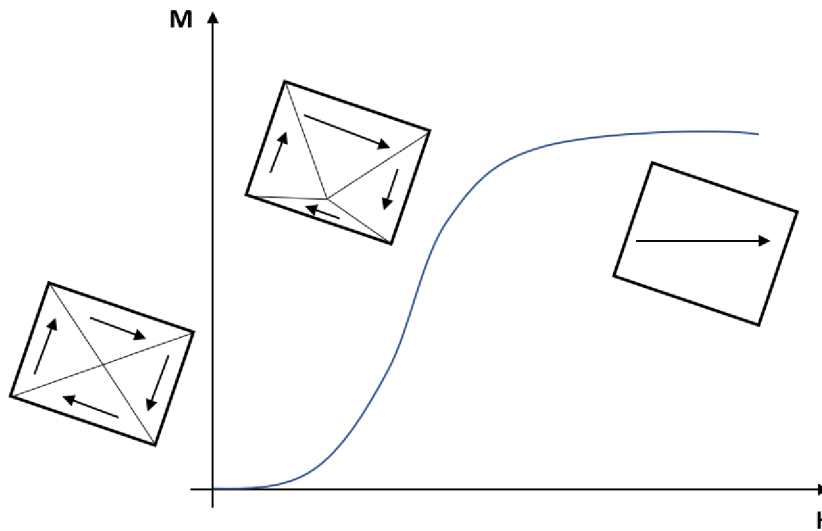

Figure 1.8.: Initial magnetization curve of a rectangular ferromagnetic structure, while the external magnetic field is applied close to the materials easy axis.

magnetization start shrinking. The growth and shrinkage are achieved by moving the domain wall. This process is completely reversible in the first phase.

Increasing the external field will move the walls far enough to encounter an imperfection (dislocations, defects, etc.). Crystal imperfections are sources of a stray field, providing magnetostatic energy. If the domain wall crosses the imperfection, this magnetostatic energy may vanish, creating a local energy minimum [16]. The domain wall often stays pinned at the imperfection, and additional energy provided by the external field is required to move the domain wall further. The imperfections usually act as nucleation centers. Also, they often form spike-like domains called Néel spikes. The additional field needed to snap the spike domains off the imperfection corresponds to the coercive field [15]. The domain wall motion is then highly dependent on the microstructure of the material.

As a result of the presence of the impurities, magnetization curves of a vast number of magnetic materials ultimately consist of a series of tiny discontinuous magnetization steps or jumps. An acoustic effect accompanies these steps caused by the snapping of the spikes. This phenomenon is known as the Barkhausen effect [14].

Eventually, the external field can be made large enough annihilate the shrinking domains and to create a single domain state in ferromagnetic body (see Figure 1.8), with the magnetization lying along the easy axis closest to the external field orientation. Further increasing the

applied field will cause another magnetization process: magnetization rotation. This process occurs in high external fields when the magnetization starts rotating along the applied field irrespective of the easy or hard axes orientation, and the sample reaches its saturated state. In the case of materials with large magnetocrystalline anisotropy, the required field may be large. If we decrease the applied field, the net magnetization decreases, and the magnetic dipoles rotate to the equilibrium positions along their easy axes. This process is again completely reversible because no domain wall propagation or domain nucleation/annihilation processes were involved [15].

Reducing the external field's magnitude back to zero will result in the demagnetizing field driven nucleation and growth of domains with opposite magnetization orientation. Therefore, the demagnetization process is caused by the demagnetizing field rather than by the mere reduction of the external field itself. An important consequence is the appearance of hysteresis (not shown in the figure) due to irreversible domain and domain wall processes.

1.4. Applications of magnetic domains and domain walls

Magnetic domains and domain walls are currently used in several technological domains, such as in sensors or information storage devices. Here, a few examples in magnetic data storage and memory devices are introduced [4].

1.4.1. Magnetic recording in hard disk drives

Magnetic storage media in the form of hard disk drives (HDD) are nowadays extensively used to store computer data, audio and video media. Likewise, magnetic tapes are also used to store huge digital data volumes [21]. Both data storages have similar data transfer mechanisms. For HDDs, a tiny read-write head is placed on top of a rotating magnetic medium, while it sweeps on top of it in order to access the information encoded in the magnetic pattern in it, consisting of a well-defined and rewritable multi-domain state. The recording medium is usually a granular thin film containing segregated single-domain particles with two possible stable configurations (magnetization "up" or "down"); a group of these particles represents a single magnetic bit, enabling to store digital information. What makes a magnetic material a great candidate for recording medium is having a wide and square hysteresis loop. Wide hysteresis loops occur in materials with high uniaxial anisotropy constant, while the squareness is achieved because of the grain geometry. A wide hysteresis loop is needed to maintain the storage's stability so that the bits will not switch due to thermal fluctuations [15]. Two configurations of domains are used. The particles' magnetization lies either in or out of the sample's plane, i.e., longitudinal or perpendicular recording mode. The perpendicular mode was introduced in 2000 and boosted the data density by orders of magnitude, bringing the possibility to make smaller bit sizes [22]. The two modes of magnetic recording are schematically shown in Figure 1.9.

Another component used to rewrite the imprinted information is a write head. The write head needs incorporate a microscale electromagnet that is capable of producing stray fields large enough to overcome the particles' coercivity, which in the employed granular films is in the order of a few Tesla.

The first commercial HDDs had an areal density of 0.1 MB/in^2. 60 years later, modern HDD devices are reaching of the order of $\sim$100 MB/in^2 and even 1 TB/in^2 [14]. Even though people
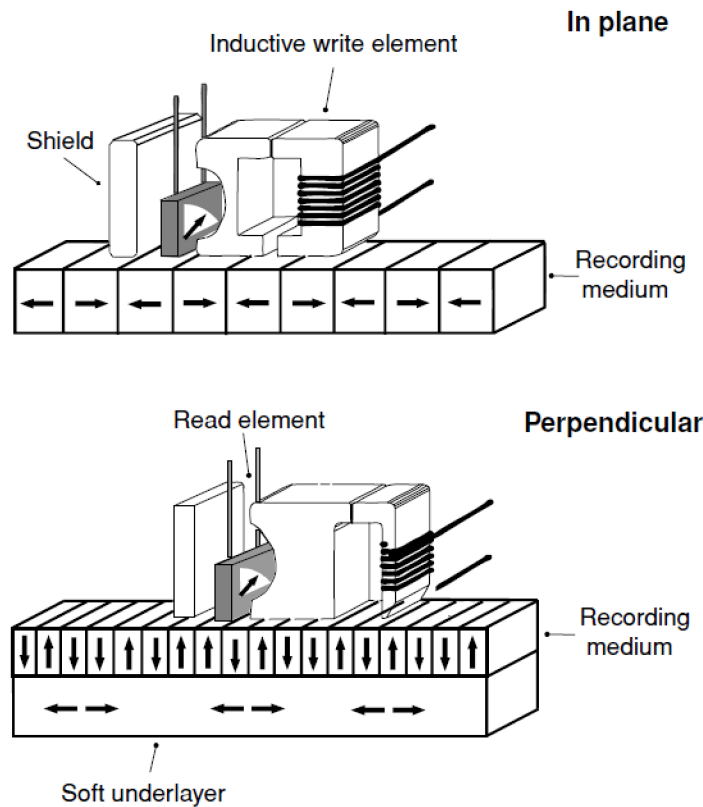
Figure 1.9.: Schematic of a recording medium with in plane and perpendicular magnetization orientation, taken from [19].

try to push the limits by increasing the information storage density via decreasing the size of bit units, while at the same time keeping their stability, there is a physical limit to the size--reduction process. Once the particles' size reaches the so-called superparamagnetic limit, the particles can no longer sustain the information, as stochastic thermal fluctuations compromise the retention of the magnetic state in the bit, causing loss of information [19].

1.4.2. Alternative magnetic memory and logic devices

A very promising an alternative approach to the problem of storing digital data in nanomagnetic systems was suggested by Parkin and his co-workers in 2008 [23]. They introduced the idea and presented a prototype of the magnetic domain-wall racetrack memory, a technology based on arrays of horizontal or vertical magnetic wires on a silicon chip. The wire comprises a series of domains with $\sim$10 to 100 domain walls. They observed that by passing a current of spin polarized electrons through the wire, they are able to control the position of the domains precisely, which enables them to write and read the information as a series of domain walls are injected and stored into the wires. One of the greatest benefits is the speed with which they can obtain the data. As the current passes and moves the domain walls, the time to read the data is less than 1-10 ns, offering clock rates that are competitive with the more established HDD technology. A second advance consists of the ability to take advantage of the third dimension, as networks of wires can be arranged along the vertical direction as well. A simple schematic of the proposed device is depicted in the Figure 1.10.

A similar advanced technology is based on magnetic skyrmions [24]. A magnetic skyrmion is a vortex-like chiral spin texture that can occur in bulk or thin film samples, see Figure 1.10

[25]. These nanomagnetic objects provide the ability to move fast under the application of currents, as well as their nanometer size, making them a potential physical object to be incorporated as information carriers in future devices. The skyrmions may be used to improve the racetrack memory technology [26]. Compared to domains, skyrmions can achieve higher data densities due to lower bit spacing, reduce power consumption thanks to their lower critical depinning current, and provide higher data stability. Furthermore, skyrmions may also be used in skyrmion logic gates or transistors.
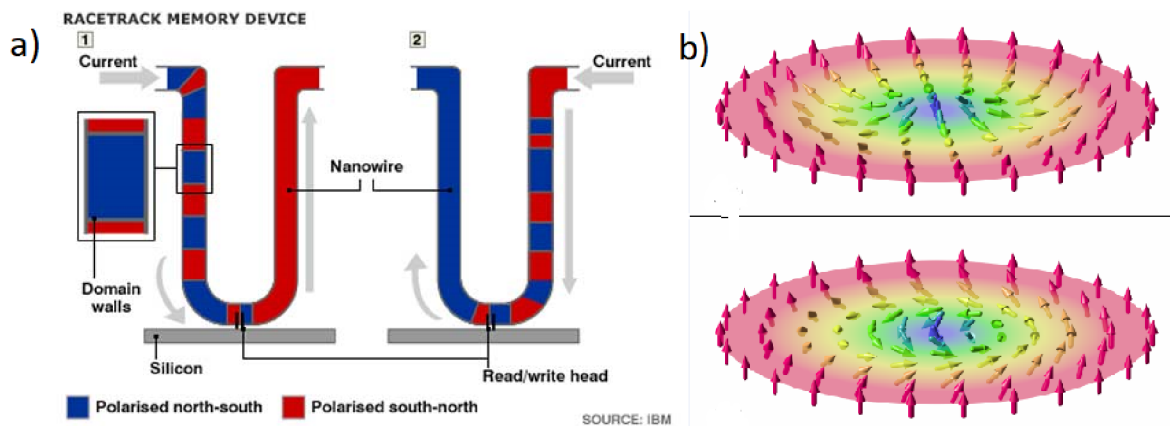

Figure 1.10.: Alternative digital data storage technologies - a) magnetic domain-wall racetrack memory device schematic, taken from [23], b) magnetic skyrmion visualization, taken from [24].

2. Magneto-optical effects

Magneto-optics is the field that studies the interaction of light with matter in a magnetic field or with material's magnetization [27]. The first magneto-optical effect was discovered in 1845 by Michael Faraday. He let a linearly polarized light beam propagate through a paramagnetic glass rod on which he applied a magnetic field along the light propagation direction, and he subsequently observed that the polarization plane of light was rotated by several degrees, in a sense of rotation that was reversed when inverting the applied field and therefore the induced magnetization in the glass. This effect is now known as the magneto-optical Faraday effect [27, 30].

A similar effect was observed 32 years later by John Kerr in reflection geometry. He noticed that a linearly polarized light reflected by a polished iron electromagnet pole had its plane of polarization rotated by tenths of degrees. Again, the sense of rotation was reversed upon switching the magnetization. This phenomenon was later named after its discoverer as the magneto-optical Kerr effect (MOKE) [28, 29].

In the original experiments of Kerr, two configurations were investigated [27]:

- the magnetization lying perpendicular to the sample surface, and

- the magnetization lying in the plane of the sample surface and contained in the plane of incident of light.

These geometries are nowadays known as the polar Kerr and longitudinal Kerr effects, respectively. Later, a third configuration was observed, in which the magnetization is oriented within the plane of the sample surface and perpendicular to the plane of incidence termed as the transversal Kerr effect.

Nowadays, magneto-optical effects are widely used as a precise and versatile method to measure magnetization in magnetic materials. A key property of magneto-optics is that the leading effects on light polarization changes are linear in magnetization [27]. This allows, for example, the measurement of magnetic hysteresis loops of different materials when sweeping an external magnetic field in a light reflection or transmission experiment [13].

Another paramount contribution of magneto-optics consists of the visualization of magnetic domains using optical microscopy techniques with polarization analysis [16]. Due to polarization changes of light during reflection or transmission, an optical contrast is measured based on its dependence on the orientation of magnetization. For metallic systems, light absorption makes transmission measurement more difficult, thus the Faraday effect may be observed only for transparent samples; hence its use is limited to ultrathin metallic films.

On the other hand, Kerr microscopy in reflection geometry is widely used to investigate bulk samples, thin films, multilayers, and more. Magneto-optics, in its earliest applications, did not show the best results for most of the materials. However, it experienced a great breakthrough after introducing digital image processing, especially the digital difference technique [16]. This approach enhances the image contrast by digitally subtracting background signals and by signal averaging.

As already mentioned, the Faraday and Kerr effects are (in the first approximation) linear in magnetization, due to the fact that magneto-optical effects only constitute a small correction to the dielectric properties of the material [30]; this means that the rotation is reversed if the magnetization is switched. However, an additional higher-order magneto-optical effect, the Voigt effect, is quadratic in magnetization, meaning that the obtained signal depends on the

magnetization axis's orientation. No contrast appears between areas with opposite magnetizations, but between areas with orthogonal spin axis orientation [30]. An additional effect useful in magnetic domain observation is a gradient effect, which depends on the spatial magnetization gradient, not on the vector orientation itself. The differences in the optical contrast of magneto-optical origin generated by the Kerr, Voigt, and gradient effects may be seen in Figure 2.1 for a silicon-iron crystal [16, 30].
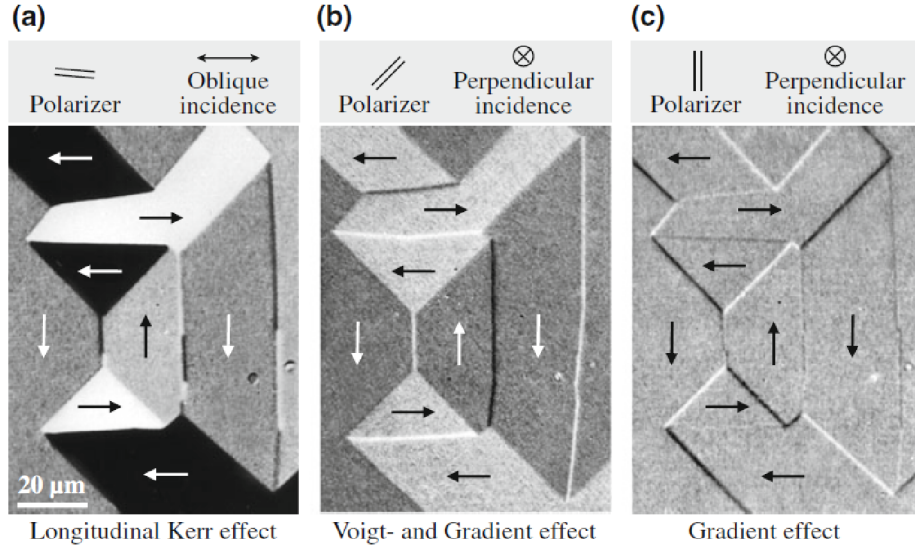

Figure 2.1.: Magnetic domain microstructure on surface of silicon-iron observed using magneto-optical- a) longitudinal Kerr effect, b) Voigt- and gradient effects, c) gradient effect. Each image is accompanied by polarizer setting as well as the incidence schematic. Taken from [30].

2.1. Electromagnetic description of light

In order to describe the interaction of light with magnetic media, we need to start with electromagnetic theory basics, the fundamentals of the electromagnetic theory consist of Maxwell's equations:

$$\nabla \cdot \boldsymbol{D} = \rho, \tag{2.1a}$$

$$\nabla \cdot \boldsymbol{B} = 0, \tag{2.1b}$$

$$\nabla \times \boldsymbol{E} = -\frac{\partial \boldsymbol{B}}{\partial t}, \tag{2.1c}$$

$$\nabla \times \boldsymbol{H} = \boldsymbol{j} + \frac{\partial \boldsymbol{D}}{\partial t}, \tag{2.1d}$$

which give us relations between macroscopic electric and magnetic fields. The electric charge ρ and electric current $\boldsymbol{j}$ densities act as sources of the electric and magnetic field, respectively. The electric field is described by both $\boldsymbol{D}$ and $\boldsymbol{E}$, which are the electric induction (or electric dis-

placement) and electric field vectors, respectively. The vectors $\boldsymbol{B}$ and $\boldsymbol{H}$ are already discussed magnetic vector fields. Each pair of fields are bound together via the material equations,

$$\boldsymbol{D} = \epsilon_0 \boldsymbol{\epsilon} \boldsymbol{E} = \epsilon_0 \boldsymbol{E} + \boldsymbol{P}, \tag{2.2a}$$

$$\boldsymbol{B} = \mu_0 \boldsymbol{\mu} \boldsymbol{H} = \mu_0 (\boldsymbol{H} + \boldsymbol{M}), \tag{2.2b}$$

where in this form, $\boldsymbol{\epsilon}$, and $\boldsymbol{\mu}$ are second-rank electric permittivity and magnetic permeability tensors, respectively. In addition, the vector fields $\boldsymbol{P}$ and $\boldsymbol{M}$ are the electric polarization and magnetization vector, respectively. If we set $\boldsymbol{j}$ and ρ to zero, the problem leads us to the following wave equation for the electric field vector $\boldsymbol{E}$,

$$\nabla^2 \boldsymbol{E} = \frac{1}{\mu_0 \epsilon_0} \frac{\partial^2 \boldsymbol{E}}{\partial t^2}, \tag{2.3}$$

where the operator ∇^2 is $\nabla^2 = \frac{\partial^2}{\partial x^2} + \frac{\partial^2}{\partial y^2} + \frac{\partial^2}{\partial z^2}$ and the speed of light in free space (vacuum) c is defined as $c^2 = 1/\mu_0 \epsilon_0$. The solution to be wave equation consists of harmonic plane waves in time t and position $\boldsymbol{r}$, in the form

$$\boldsymbol{E}(\boldsymbol{r}, t) = \boldsymbol{E_0} \exp\{i(\boldsymbol{k} \cdot \boldsymbol{r} - \omega t)\}, \tag{2.4}$$

where the vector $\boldsymbol{E_0} = (E_{x0}, E_{y0}, E_{z0})$ is the amplitude vector, ω is the angular frequency, and $\boldsymbol{k}$ is the wave number vector, determining the direction of propagation of the light. The $\boldsymbol{k}$ vector's magnitude is connected with the wavelength λ via $|\boldsymbol{k}| = 2\pi/\lambda$, also $|\boldsymbol{k}| = \omega/c$.

Substituting the wave equation solution back to Maxwell's equations, we find out that even the $\boldsymbol{B}$-field is a plane wave,

$$\boldsymbol{B}(\boldsymbol{r}, t) = \boldsymbol{B_0} \exp\{i(\boldsymbol{k} \cdot \boldsymbol{r} - \omega t)\}. \tag{2.5}$$

Furthermore, the $\boldsymbol{E}$ and $\boldsymbol{B}$ fields, describing the electromagnetic wave, are simultaneously perpendicular to each other and the direction of propagation. We write

$$\boldsymbol{k} \times \boldsymbol{E} = \omega \boldsymbol{B}. \tag{2.6}$$

When considering light propagation in a material medium, these results can be generalized by introducing the refractive index n, which is given by

$$n = \frac{c}{v}, \tag{2.7}$$

where v is the modulus of the (phase) propagation speed of the electromagnetic wave in the material

$$v = \frac{1}{\sqrt{\epsilon_0 \epsilon \mu_0 \mu}}, \tag{2.8}$$

thus the refractive index is [30]

$$n = \sqrt{\epsilon \mu}. \tag{2.9}$$

2.2. Light polarization

As mentioned in the previous section, the electromagnetic wave is a transverse wave, with $\boldsymbol{E}$- and $\boldsymbol{B}$- fields having an oscillatory nature. When we describe the interaction of light with matter, we often limit the description to electric fields. Firstly, we are allowed to do so because the magnetic part may be easily calculated using Equation (2.6) and secondly because the effect of $\boldsymbol{E}$-field is much stronger than that of the $\boldsymbol{B}$-field. When defining the polarization, we take advantage of the transverse character of the light. Upon considering light propagating along the $z-$axis, the $\boldsymbol{E}$-vector will lie in the $xy-$plane.

If we do not have any special light source or optical element (such as a laser), the light will be unpolarized in most cases. Unpolarized light beams imply that the trajectory written by the tip of the $\boldsymbol{E}$-vector is quick and unpredictable. In contrast with the polarized light, whose time-dependent trajectory in the transverse plane propagating with light is generally an ellipse in the most general case (hence the term elliptically polarized light) [31].

To derive the general elliptical polarization state, we split the $\boldsymbol{E}$-vector into the x and y components. We shall take the real part of the equation describing the $\boldsymbol{E}$-field because the electric field's intensity is a quantity that can be directly measured; therefore, it has to be real. The individual components are:

$$E_x = E_{0x} \cos(k_z \cdot z - \omega t + \phi_x), \tag{2.10a}$$
$$E_y = E_{0y} \cos(k_z \cdot z - \omega t + \phi_y), \tag{2.10b}$$

where the ϕ_x, ϕ_y phase quantities in the argument of the cosine are the phase shifts of each component. It is beneficial to define $\Delta\phi = \phi_y - \phi_x$ as the phase shift difference. When combining the two components, it is possible to derive the following equation:

$$\left(\frac{E_x}{E_{0x}}\right)^2 + \left(\frac{E_y}{E_{0y}}\right)^2 - 2\frac{E_x}{E_{0x}}\frac{E_y}{E_{0y}}\cos(\Delta\phi) = \sin^2(\Delta\phi). \tag{2.11}$$

This equation describes an ellipse in the (E_x, E_y) plane, thus demonstrating that the most general polarization geometry of a fully polarized electromagnetic wave is an ellipse.

There are two special cases of polarization state:

1. If $\Delta\phi = n \cdot \pi, n \in \mathbb{Z}$:
   The Equation (2.11) is simplified into the following form,

   $$E_y = \pm\frac{E_{0y}}{E_{0x}}E_x, \tag{2.12}$$

   which illustrates a linear dependence between the $x-$ and $y-$components of the electric field; thus, we call this polarization state a linear polarization. The slope α is given by $\alpha = E_{0y}/E_{0x}$.

2. If $\Delta\phi = (2 \cdot n - 1) \cdot \pi/2, E_{0x} = E_{0y}, n \in \mathbb{Z}$:
   After substituting, we get:

   $$E_x^2 + E_y^2 = E_{0x}^2 = E_{0y}^2, \tag{2.13}$$

which is the equation of a circle in the (E_x, E_y) plane; therefore, the resultant polarization is called circular polarization. We often stick just to $n = 0, 1$, which means $\Delta\phi = \pi/2, -\pi/2$. The case of $\Delta\phi = -\pi/2$ corresponds to the y-component being 90° ahead, which results in the $\boldsymbol{E}$-vector rotating clockwise. We term this case as right-circularly polarized light (RCP). The other case, in which $\Delta\phi = \pi/2$, results in anticlockwise rotation, thus being named as left-circularly polarized light (LCP).

In more general cases, the polarization is elliptic. The following quantities characterize the elliptic polarization:

- the ratio between amplitudes of y- and x- components, $\tan\Omega = E_{0y}/E_{0x}$,

- the phase difference $\Delta\phi$,

- the azimuth angle θ, which refers to the rotation of the major axis of the ellipse,

- the ellipticity ξ, which tells us "how much elliptical" is the trajectory in the (E_x, E_y) plane plane, $\tan\xi = b/a$, and

- the sense of rotation (similar to circular polarization).

All mentioned cases of light polarization, together with their characteristics, are shown in the Figure 2.2.
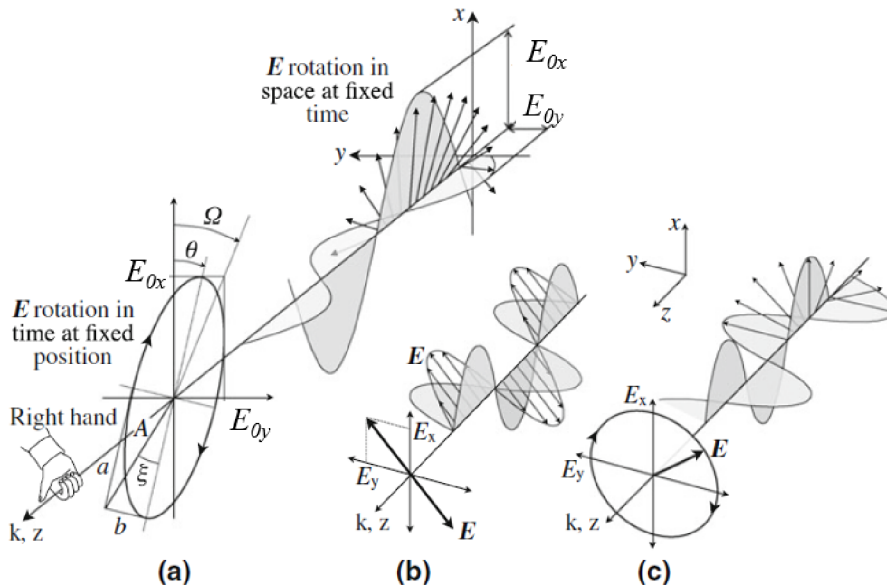

Figure 2.2.: Visualization of light polarization states together with its characteristics - a) elliptical polarization, b) linear polarization, c) circular polarization. Taken and edited from [30].

When describing a light polarization, it is beneficial to use the Jones formalism. The so-called Jones vector is represented by a column vector which consists of a compact representation of the $\boldsymbol{E}$-vector components,

$$J = \begin{pmatrix} E_x \\ E_y \end{pmatrix} = \begin{pmatrix} E_{0x}\, e^{i\phi x} \\ E_{0y}\, e^{i\phi y} \end{pmatrix}, \tag{2.14}$$

where we got rid of the term expressing spatial and time dependent oscillatory behavior, $\exp\{i(k_z z - \omega t)\}$. The key feature of the Jones vector is that it describes the amplitude and phase of the polarized light in the (E_x, E_y) plane. Moreover, because what we are interested in is just a relative amplitude, we normalize the Jones vector, i.e., $J^* \cdot J = 1$, where the symbol "$*$" represents the complex conjugate.

It is advantageous to use the Jones formalism to map the polarization state of light as it interacts with individual optical elements along the optical path. In this formalism, each optical element is represented by a 2×2 Jones matrix which induces modifications in the incoming, original polarization state. For an incident polarization state J, which is sent through an optical element A, we write the resultant polarization state J' as

$$J' = A \cdot J = \begin{pmatrix} a_{11} & a_{12} \\ a_{21} & a_{22} \end{pmatrix} \begin{pmatrix} J_1 \\ J_2 \end{pmatrix}, \tag{2.15}$$

where the 2×2 matrix in Equation (2.15) is associated to the particular optical element. The mathematical description of a number of exemplary polarization states (e.g., linear, circular, elliptical) and 2×2 matrix representations of common optical components (e.g., polarizer, phase retarder) are summarized in the Appendix A of this thesis.

Likewise, polarization changes of light upon reflection or transmission from a material can also be represented within the Jonex formalism. The change of polarization state caused by a reflection or transmission is equally described by corresponding matrices:

$$R = \begin{pmatrix} r_{xx} & r_{xy} \\ r_{yx} & r_{yy} \end{pmatrix}, T = \begin{pmatrix} t_{xx} & t_{xy} \\ t_{yx} & t_{yy} \end{pmatrix}. \tag{2.16}$$

The elements within the matrices are termed as the reflection $r_{ij} = E_i^r/E_j$ and transmission $t_{ij} = E_i^t/E_j$ electric field amplitude coefficients. The electric field amplitude coefficients give us a ratio of reflected (or transmitted) light amplitudes E_i^r (or E_i^t) polarized along $i = \{x, y\}$ - axis to the incident light amplitude E_j polarized along $j = \{x, y\}$ - axis.

2.3. Dielectric permittivity

The electromagnetic wave sent on a material's surface causes electrons in the atomic orbitals to oscillate. This oscillatory motion of an electric dipole (negatively charged electron bound to a positive proton) is a secondary wave source. As the incident wave excites other electrons' oscillations, the secondary waves combine according to Huygens' principle. The $\boldsymbol{D}$-vector determines the direction of the electron oscillation, the electric displacement vector, according to Equation (2.2a).

The interaction between light and matter is represented in the framework of electromagnetic theory via the dielectric permittivity tensor which for non-magnetic materials reads as

$$\boldsymbol{\epsilon}_{cryst} = \boldsymbol{\epsilon}^0 + \boldsymbol{\epsilon}_{br} + \boldsymbol{\epsilon}_{oa}, \ \boldsymbol{\epsilon}^0 = \begin{pmatrix} \epsilon_{iso} & 0 & 0 \\ 0 & \epsilon_{iso} & 0 \\ 0 & 0 & \epsilon_{iso} \end{pmatrix}, \tag{2.17}$$

where $\boldsymbol{\epsilon}^0$ is an isotropic tensor, $\boldsymbol{\epsilon}_{br}$ is a traceless matrix describing crystalline birefringence,

and ϵ_{oa} is an optical activity tensor [30]. If we consider an isotropic and non-magnetic material with the only ϵ^0 being non-zero, we see that the $\boldsymbol{D}$- and $\boldsymbol{E}$- vectors are parallel to each other (the dielectric tensor reduces to a scalar). Nevertheless, in the general case, the $\boldsymbol{D}$- and $\boldsymbol{E}$-vectors have different orientations.

In order to describe the magnetization-induced changes in the permittivity, the dielectric tensor is expanded in terms that are first-order and second-order in magnetization (neglecting higher order terms, since magneto-optical effects are generally small). In a cubic magnetic material, the permittivity tensor might be expressed by the following sum of terms

$$\boldsymbol{\epsilon} = \epsilon_{iso} \begin{pmatrix} 1 & -Q_V m_3 & iQ_V m_2 \\ iQ_V m3 & 1 & -iQ_V m_1 \\ -iQ_V m_2 & iQ_V m_1 & 1 \end{pmatrix} + \begin{pmatrix} B_1 m_1^2 & B_2 m_1 m_2 & B_2 m_1 m_3 \\ B_2 m_1 m_2 & B_1 m_2^2 & B_2 m_2 m_3 \\ B_2 m_1 m_3 & B_2 m_2 m_3 & B_1 m_3^2 \end{pmatrix}. \quad (2.18)$$

The first term describes a dielectric tensor including linear magneto-optical Kerr effects (with matrix elements linear in magnetization), where m_i are the normalized Cartesian components magnetization defined as $\boldsymbol{m} = \boldsymbol{M}/M_s$ along the cubic axes, and Q_V is a complex material parameter known as a Voigt constant, denoting the strength of linear magneto-optical effects. By considering only the first term in Equation (2.18), the material Equation (2.2a) may be rewritten as [16]

$$\boldsymbol{D} = \epsilon_0 \epsilon_{iso} \left(\boldsymbol{E} + iQ_V \boldsymbol{m} \times \boldsymbol{E} \right). \quad (2.19)$$

Equation (2.19) points to the idea that the magnetization vector $\boldsymbol{m}$ actuates in similar fashion as a Lorentz force in the material's electrons, the origin of this force being light illumination.

The second term in equation (2.18) represents the Voigt effect (quadratic in magnetization); the complex constants B_1 and B_2 are also material parameters and are equal in isotropic or amorphous materials.

2.4. Description of Kerr effects

Although the dielectric permittivity tensor describes a connection of the magnetization and optical properties, it is not really a quantity that can be directly measured in an experiment. Instead, we may observe its effect once the light gets reflected (or transmitted) and describe the phenomena using magnetization dependant Fresnel reflection (or transmission) coefficients.

The mathematic approach to the problem begins by considering the Maxwell equations and derived wave equation for the $\boldsymbol{E}$-field. Considering plane wave solutions for a given dielectric tensor $\boldsymbol{\epsilon}$, on reaches an eigenvalue and eigenstate problem for the $\boldsymbol{k}$-vectors (or refractive indices) and polarization states ($\boldsymbol{E}$-field eigenvectors) of the propagating waves [27].

In further, we will use another convention used in polarization optics. We define the s-polarization and p-polarization, which form a basis expressed in Jones formalism:

$$E_s = \begin{pmatrix} 1 \\ 0 \end{pmatrix}, E_p = \begin{pmatrix} 0 \\ 1 \end{pmatrix}. \quad (2.20)$$

The subscript s stands for "senkrecht," perpendicular in German; the s-polarization represents light having its polarization plane perpendicular to the plane of incidence. The p-polarized light, from the German "parallel," describes light polarized in the plane of incidence. This

polarization basis is advantageous to describe MOKE experimental geometries for an arbitrary angle of incidence of light. Both polarizations are shown in a schematic Figure 2.3.
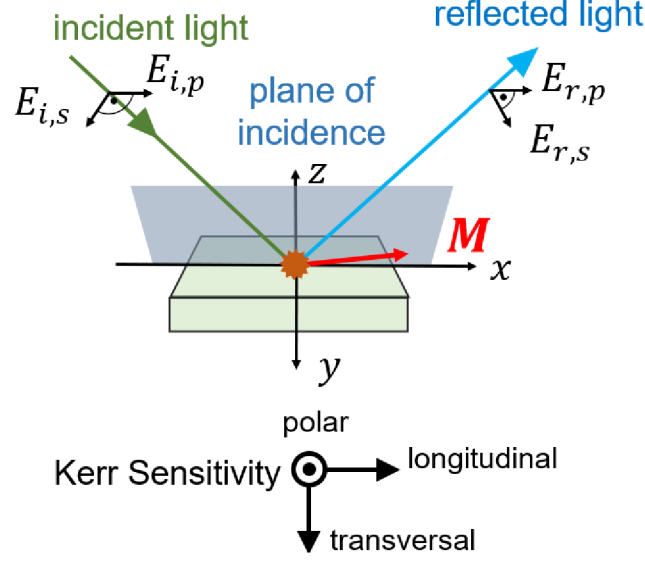

Figure 2.3.: Introduction of used light reflection convention using s- and p- light polarizations as well as the plane of incidence, $xyz-$coordinate system, and corresponding Kerr sensitivity schematic.

Upon solving the eigenvalue-eigenvector problem, and imposing the continuity relations of the field vectors and the interface between the incident medium and the magnetic medium, the Fresnel coefficients can be calculated [30]. If we take only terms linear in magnetization, the reflection Fresnel coefficients are [30]:

$$r_{ss} = \frac{n_0 \cos\theta_0 - n_1 \cos\theta_1}{n_0 \cos\theta_0 + n_1 \cos\theta_1}, \tag{2.21a}$$

$$r_{sp} = \frac{in_0 n_1 \cos\theta_0 \left(m_z \cos\theta_1 + m_x \sin\theta_1\right) Q_V}{\left(n_1 \cos\theta_0 + n_0 \cos\theta_1\right)\left(n_0 \cos\theta_0 + n_1 \cos\theta_1\right) \cos\theta_1}, \tag{2.21b}$$

$$r_{pp} = \frac{n_1 \cos\theta_0 - n_0 \cos\theta_1}{n_1 \cos\theta_0 + n_0 \cos\theta_1} - \frac{2in_0 n_1 \cos\theta_0 \sin\theta_1 m_y Q_V}{n_1 \cos\theta_0 + n_0 \cos\theta_1}, \tag{2.21c}$$

$$r_{ps} = \frac{in_0 n_1 \cos\theta_0 \left(m_z \cos\theta_1 - m_x \sin\theta_1\right) Q_V}{\left(n_1 \cos\theta_0 + n_0 \cos\theta_1\right)\left(n_0 \cos\theta_0 + n_1 \cos\theta_1\right) \cos\theta_1}. \tag{2.21d}$$

For deriving these equations, the Snell's law $n_0 \sin\theta_0 = n_1 \sin\theta_1$, was used, where θ is the angle of incidence. The subscript "0" indicates incident light half-space, whereas subscript "1" the materials half-space. In this convention, we take both angles from the surface normal.

We can summarize the coefficients using Fresnel reflection matrix written in the Jones formalism [32],

$$R = \begin{pmatrix} r_{ss} & r_{sp} \\ r_{ps} & r_{pp} \end{pmatrix} = \begin{pmatrix} r_s & Am_x + Bm_z \\ -Am_x + Bm_z & r_p + Cm_y \end{pmatrix}. \tag{2.22}$$

Other quantities in the equation above are the magnetization independent complex reflectivity terms r_s and r_p. Also, complex coefficients A, B, and C which are usually small compared to r_s and r_p when we measure Kerr effects.

The Fresnel coefficients strongly depend on experimental conditions (for instance, angle of incidence); this dependence can be further used to separate individual magnetization dependant components.

As mentioned earlier, the Faraday and Kerr effects are rotational magneto-optical effects linear in magnetization, applying in light transmission and reflection, respectively [30]. The Faraday effect, thus, can be observed only in transparent samples or very thin ones. On the other hand, the Kerr effect applies in a variety of samples, including any metallic or other light-absorbing materials. Even though both effects result from the same phenomenology, we will further discuss the Kerr effect because our focus is mainly on metals.

The Kerr effect might be explained correctly using magneto-optical tensor, Maxwell's equations, adequate boundary conditions, and arguments based on the Lorentz force concept. Even though we may use this semiclassical explanation, the magneto-optical effects originate from quantum mechanics and should be dealt with as such (see Section 2.5).

Consider a magnetic material; the incident light with its $\boldsymbol{E}$-vector interacts with the magnetization $\boldsymbol{m}$ according to equation (2.19), causing a secondary motion of electrons given by $\boldsymbol{v}_{lor} = -\boldsymbol{m} \times \boldsymbol{E}$. The Huygens' principle then gives rise to the amplitude of light due to the Kerr effect called a Kerr amplitude $\boldsymbol{R}_K$. The regularly reflected light component is polarized in the same plane as the incident light, and we call this component regularly reflected amplitude $\boldsymbol{R}_N$. The superposition of both amplitudes hence leads to linear dependence on magnetization if they are in phase. In case the amplitudes are not in phase, the emerging light is elliptically polarized, which can be changed back to linearly polarized using a compensator. The mentioned quantities are depicted in Figure 2.4.

There are three geometries for measuring the Kerr effect, which differ in the relative orientation of a plane of incidence, initial polarization plane direction, and magnetization [16], see Figure 2.4.

1. Longitudinal effect: the magnetization lies in the plane of the sample and is parallel to the plane of incidence. In the case of $\theta_0 = 0°$, the secondary electron motion either reduces to zero or creates a Kerr amplitude $\boldsymbol{R}_K$ parallel to the regularly reflected amplitude $\boldsymbol{R}_N$, resulting in no contrast. To observe the longitudinal effect, the oblique incidence needs to be chosen. The rotational effect is possible for both, polarization plane lying parallel or perpendicular to the incidence plane.

2. Polar effect: the magnetization lies in the sample normal. If $\theta_0 = 0°$, the rotation is the same for all linear polarizations due to the symmetry; it is also the strongest at normal incidence.

3. Transverse effect: the magnetization lies in the plane of the sample and is perpendicular to the plane of incidence. Incident light linearly polarized along the incidence plane results in the Kerr amplitude parallel to the reflected amplitude, which means no polarization plane rotation. To obtain a detectable rotation, the incident polarization must lie between perpendicular and parallel to the incidence plane. For incident p-polarization, the transverse effect (m_y magnetization) does not induce any rotation or ellipticity, but only a modulation of the reflected light intensity – see Equation (2.22).
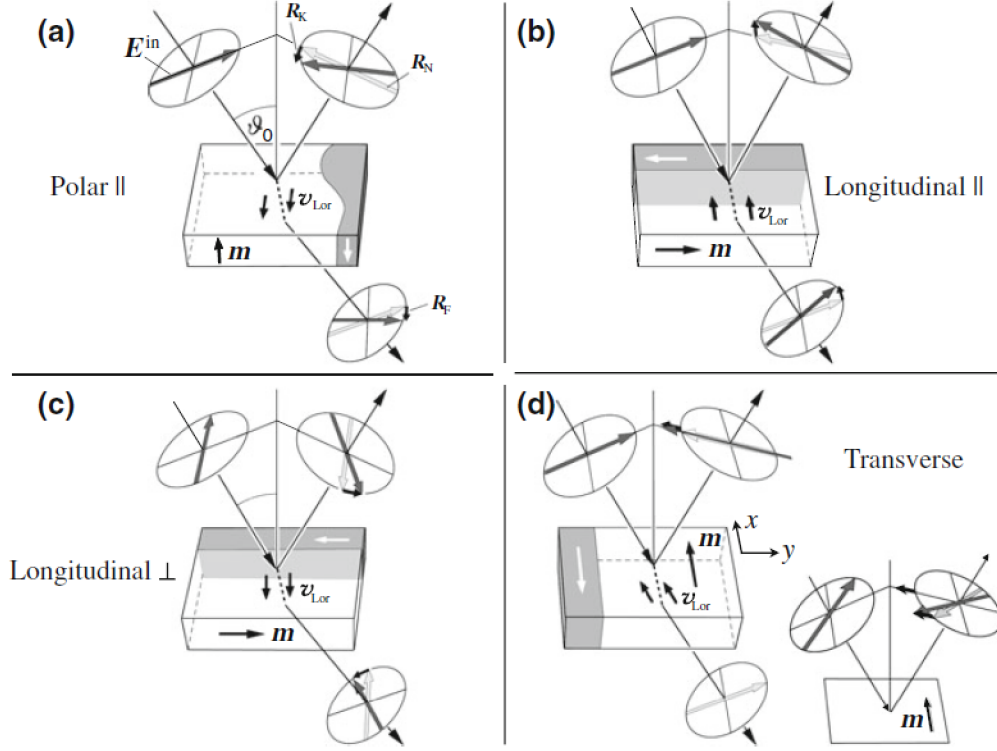
Figure 2.4.: Schematic of magneto-optical Kerr effects geometries - a) polar Kerr effect: linearly polarized light at normal incidence, out of plane magnetization orientation, b) longitudinal Kerr effect: linearly polarized light parallel to the plane of incidence, magnetization lays in plane of the sample, and is parallel to the plane of incidence, c) longitudinal Kerr effect: linearly polarized light perpendicular to the plane of incidence, magnetization lays in plane of the sample, and is parallel to the plane of incidence, d) transversal Kerr effect: incident light linearly polarized parallel to the plane of incidence, the magnetization is in plane of the sample but perpendicular to the plane of incidence. Taken from [30].

2.5. Microscopic origin of magneto-optical effects

If we consider just the first term of the equation (2.18) and perpendicular light incidence, we may derive an eigenvalue equation $\epsilon E = n^2 E$, from which we get the following eigenmodes [19] for the polarization state of light propagating in the magnetic medium

$$E_1 = \begin{pmatrix} 1 \\ i \end{pmatrix}, E_2 = \begin{pmatrix} 1 \\ -i \end{pmatrix}. \tag{2.23}$$

These two eigenmodes represent left and right circularly polarized light, and because they have different eigenvalues, i.e., refraction indices, they will also propagate through the material at different velocities (for an opaque medium, they will also experience a slightly different absorption). Thus, both Kerr and Faraday effects may be thought of as a birefringence of circularly polarized light or circular birefringence [19].

The microscopic explanation requires an assumption of both exchange splitting and spin-orbit splitting. For simplicity, let us consider observing the polar Kerr effect at normal incidence with magnetization along the surface normal [33].

The exchange splitting originates from the Coulomb repulsion and Pauli's exclusion principle, which forbids pair of electrons to be in the same quantum state. This means that the energies corresponding to a triplet $\uparrow_i\uparrow_j$ and singlet $\downarrow_i\uparrow_j$ states have to be different; indices i and j represent different spins configurations of adjacent atoms [15]. The exchange splitting results in the spin-up population of the individual atomic orbitals having different energy than the spin-down population.

Spin-orbit coupling is a relativistic interaction that can be explained if we consider an electron orbiting around the nucleus. In a coordinate system attached to the electron, it seems like the nucleus revolves around it. This circular motion reminds us of a current loop generating a magnetic field. This magnetic field interacts with the electron's magnetic moment, connected to its spin, which results in a splitting of the atom's energy levels [19]. We call this effect the spin-orbit splitting. The magnitude of the spin-orbit coupling is proportional to the atomic number of the nucleus Z; hence it is the strongest in heavy elements.

In our simple case, we visualize only initial d and final p states because the d states are responsible for the ferromagnetic behavior. We will also neglect exchange splitting of the unoccupied p states.

The incident linearly polarized light may be represented by a superposition of eigenmodes from equation (2.23). Each eigenmode represents an individual photon with orbital quantum number $l = 1$ and magnetic quantum number $m_l = \pm 1$, where each sign corresponds to one photon helicity. The selection rules allow transitions from the occupied d (i.e. $l = 2$) states to unoccupied p (i.e. $l = 1$) states. Furthermore, the law of conservation of the angular momentum, i.e., the m_l selection rule $\Delta m_l = \pm 1$, must be obeyed, as well as the l selection rule $\Delta l = \pm 1$.

The schematic of energy levels together with possible electronic transitions is shown in Figure 2.5. The states are labeled using the terminology $|l\ m_l \uparrow\rangle$ and $|l\ m_l \downarrow\rangle$, where symbols $\uparrow$ and $\downarrow$ again represent spin up and down, respectively. Energy levels for spin up are on the left, and in the middle, there are energy levels for a spin down; they are separated because of the exchange splitting. The finer separation of levels is caused by spin-orbit splitting.

The vertical lines in the Figure 2.5 correspond to all possible transitions, including the conservation of spin during electric dipole transitions ($d \rightarrow p$). The schematic on the right shows a resultant absorption spectrum for both circular polarizations. As discussed before, this circular polarization-dependent light absorption is known as circular dichroism.

The circular polarizations recombine after the reflection, so the resultant light is again linearly polarized. However, due to the circular birefringence, the plane of polarization seems rotated with respect to incident one.

A more detailed elaboration on description magneto-optical Kerr effects using quantum mechanics theory is provided in [34], and [33].
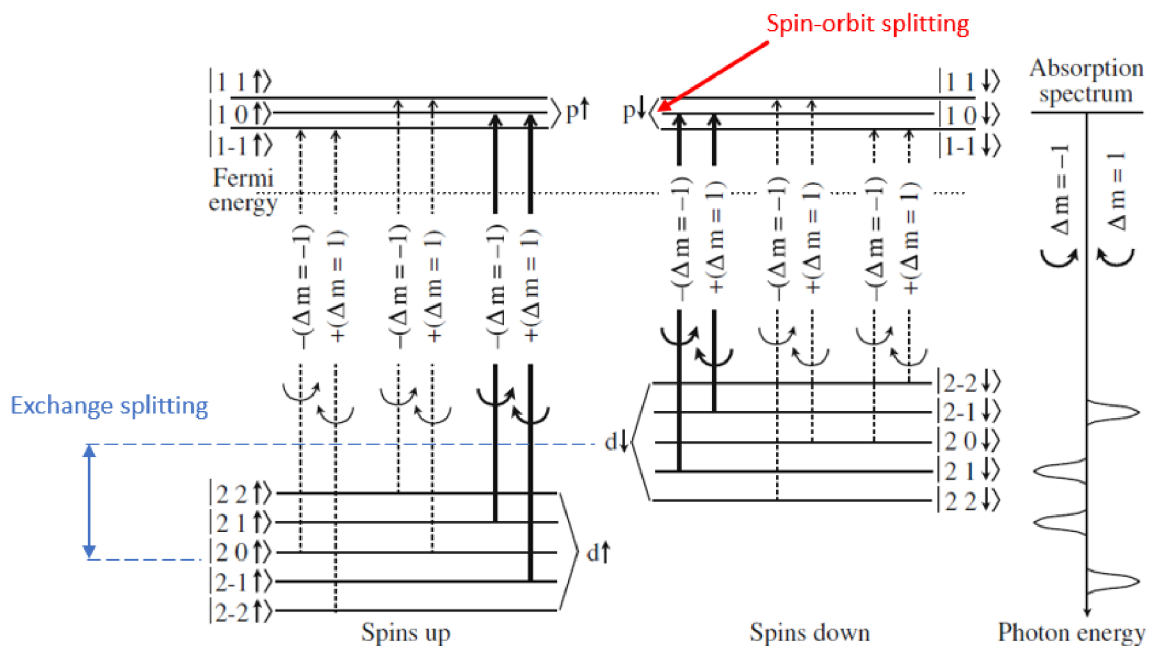
Figure 2.5.: Energy diagram of possible electronic transitions while taking into account the $\Delta l = \pm 1$ and $\Delta m_l = \pm 1$ selection rules. We are considering exchange splitting of the d states, and spin-orbit splitting of both d and p states. Circular polarizations with different helicity excite specific states according to the selection rules, which leads to different absorption spectrum for both circular polarizations. Edited and taken from [19].

3. Vector magnetometry of magnetic domains using MOKE

Gaining information about the connection of the magnetic microstructure of a material and its magnetization curve is challenging in general, particularly because the important role of chemical composition inhomogenities and defects (e.g., domain wall pinning points) in the magnetization processes. To some extent, it is quite simple to predict the magnetization distribution or domain configuration of simple specimens with large and dominant magnetocrystalline anisotropy constants in zero externally applied magnetic field. However, things get more complicated when we apply a magnetic field, the specimen contains locally stressed regions, when we deal with an amorphous sample, or when we scale down the spatial dimensions of structures of interest.

From all approaches used for domain observation, not all allow quantitative magnetization analysis. The common problem is that most techniques exhibit either a non-linear or indirect response to magnetization. One of the methods suitable for quantitative magnetometry is provided by magneto-optics.

This chapter presents a strategy to perform quantitative vector magnetometry of ferromagnetic domains using magneto-optical microscopy. The proposed analysis is performed on patterned micrometer-sized permalloy (NiFe) structures and ferromagnetic FeRh thin films.

3.1. Kerr signal separation

In the following, a rather schematical description will be provided on how the signal proportional to linear magnetization components can be measured using magneto-optical Kerr effects in the optical microscope setting. We will focus on geometry in which we measure the horizontal component of magnetization using the longitudinal Kerr effect, i.e., the so-called longitudinal sensitivity.

In a typical experiment, arbitrarily polarized or unpolarized light from a source is polarized by a linear polarizer, set so that incident light on the sample is p-polarized; this can be represented by p-polarized Jones vector E_i:

$$E_i = \begin{pmatrix} 0 \\ 1 \end{pmatrix}. \tag{3.1}$$

The incident light interacts with the specimen surface and gets reflected, i.e., reflection matrix R introduced in equation (2.22) acts on the E_i vector as follows:

$$E' = R \cdot E_i = \begin{pmatrix} r_{ss} & r_{sp} \\ r_{ps} & r_{pp} \end{pmatrix} \begin{pmatrix} 0 \\ 1 \end{pmatrix} = \begin{pmatrix} r_{sp} \\ r_{pp} \end{pmatrix}. \tag{3.2}$$

Next, the polarization vector E' would have to pass through the compensator (quarter-wave plate), but for now, we simplify the problem and do not take it into account. Its role is to adjust the real and imaginary part of the reflected light vector E' in order to maximize the measured magneto-optical contrast [30].

After reflection, the light goes to the analyzer, which is a second linear polarizer. Here let α be an the orientation of the analyzer axis with s-polarization. The analyzer is set very close to the extinction position with respect to the polarizer, i.e., $\alpha = \delta$, where δ is a small angle.

Let us take the analyzer Jones matrix A with an angle α (see Appendix A), the output Jones vector is then

$$E_f = A \cdot E' = \begin{pmatrix} \cos\alpha^2 & \cos\alpha\sin\alpha \\ \cos\alpha\sin\alpha & \sin\alpha^2 \end{pmatrix} \begin{pmatrix} r_{sp} \\ r_{pp} \end{pmatrix} \approx \begin{pmatrix} 1 & \delta \\ \delta & 0 \end{pmatrix} \begin{pmatrix} r_{sp} \\ r_{pp} \end{pmatrix} = \begin{pmatrix} r_{sp} + \delta r_{pp} \\ \delta r_{sp} \end{pmatrix}. \quad (3.3)$$

Where we took $\alpha = \delta$ and assumed $\sin\delta \sim \delta$ and $\cos\delta \sim 1$, taking only the first terms of the Taylor expansion and omitting the rest. Next, we have to calculate the intensity I by squaring the Jones vector, because it is what we actually measure in the experiment.

$$I = |E_f|^2 = |r_{pp}|^2 \left(|\delta + am_x + bm_z|^2 + |\delta(am_x + bm_z)|^2 \right) \approx |r_{pp}|^2 |\delta + am_x + bm_z|^2, \quad (3.4)$$

where the ratio r_{sp}/r_{pp} was simplified according to Equation (2.22)

$$\frac{r_{sp}}{r_{pp}} = \frac{Am_x + Bm_z}{r_p + Cm_y} \approx \frac{Am_x + Bm_z}{r_p} = am_x + bm_z, \quad (3.5)$$

where a and b are complex values and small, depending on the refractive indices of the incident and magnetic medium, Voigt constant, and the angle of incidence, see Equation (2.21). In addition, the term in Equation (3.4) that is quadratic both in δ and a, b was neglected. If we take a square of the expression on the right in the Equation (3.4) and omit again the quadratic terms in a and b, which are very close to zero, we get

$$I = |r_{pp}|\delta^2 \left(1 + \frac{\mathrm{Re}(a)}{2\delta}m_x + \frac{\mathrm{Re}(b)}{2\delta}m_z \right). \quad (3.6)$$

The expression in Equation (3.6) illustrates that the leading terms (in a, b) of the MOKE signal within this detection geometry are proportional to the longitudinal and polar magnetization.

Another step is the separation of the individual magnetization components. The key to this approach is changing the angle of incidence because the complex coefficients a and b have different symmetries with respect to the inversion of the angle of incidence. The coefficient a changes sign when inverting the angle of incidence as can be concluded from the definition of r_{sp} in Equation (2.21b). On the other hand, the coefficient b keeps its sign when inverting the angle of incidence, due to the evenness of the cosine function.

Let us take the intensity of the light I_1 with a certain angle of incidence, and intensity I_2 with an inverted angle of incidence

$$I_1 = I_0 \left(1 + \frac{\mathrm{Re}(a)}{2\delta}m_x + \frac{\mathrm{Re}(b)}{2\delta}m_z \right), \quad (3.7a)$$

$$I_2 = I_0 \left(1 - \frac{\mathrm{Re}(a)}{2\delta}m_x + \frac{\mathrm{Re}(b)}{2\delta}m_z \right). \quad (3.7b)$$

Thus, if we measure the signal with the original angle of incidence and then the inverted one and subtract them, we can extract the longitudinal component of the magnetization. In the other case, if we add the two signals, we get the polar component of magnetization. The polar Kerr signal is, of course, maximum when the incoming light is nearly at normal incidence.

To measure the transverse magnetization component m_y, it is possible to follow the same strategy either rotating the whole sample by 90° or rotating the incidence plane. The first option is not recommended since it will not be trivial to set the sample correctly. The other strategy is better achievable because all it needs is to use a light source (typically light-emitting diode, LED) arranged in a horizontal and vertical line, see Figure 3.1.
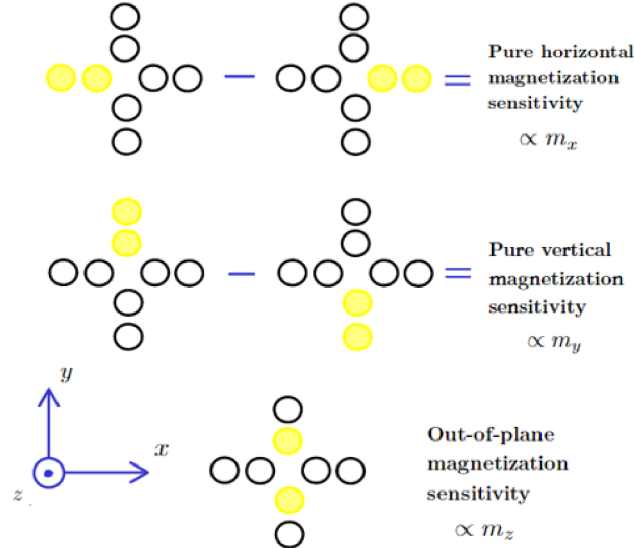

Figure 3.1.: LED lamp configuration schematic, which allows separating signal purely proportional to longitudinal, transversal or polar sensitivity.

3.2. Kerr microscope

In previous sections, we already suggested a few principles of how is the measurement of Kerr effects done. The following section submits a rather comprehensive description of the simple working principle of the Kerr microscope.

In general, wide-field Kerr microscopes are light reflection-based microscopes with strain--free optics necessary for polarization microscopy since strain in optical components causes polarization changes [30]. The schematic of the ray paths is in the Figure 3.2.

The Kerr microscope used for measurements in this work is an optical microscope from Evico Magnetics including polarization optics and using an array of white light stable LED lamps [35]. The instrument is equipped with $20\times$ and $50\times$ magnification objectives from Zeiss, suitable for polarization-dependent measurements. In addition, a rotatable electromagnet allows applying fields up to 330 mT in the in-plane direction.

The light is focused and polarized via a polarizer that has a set position. The magneto-optical Kerr effect induces rotation of the polarization plane as the light is reflected. Then the light passes through an adjustable compensator, which allows improving the Kerr signal since it removes the ellipticity of the polarized light if properly set. Finally, rotating an analyzer that is nominally set close to the extinction causes contrast in the resultant image. Good conditions for Voigt- and gradient microscopy of in-plane domains are also possible thanks to centered aperture iris.

Because Kerr contrast is rather weak in principle, image processing is required to enhance the contrast. The ideal technique to use in magnetic materials is difference imaging because
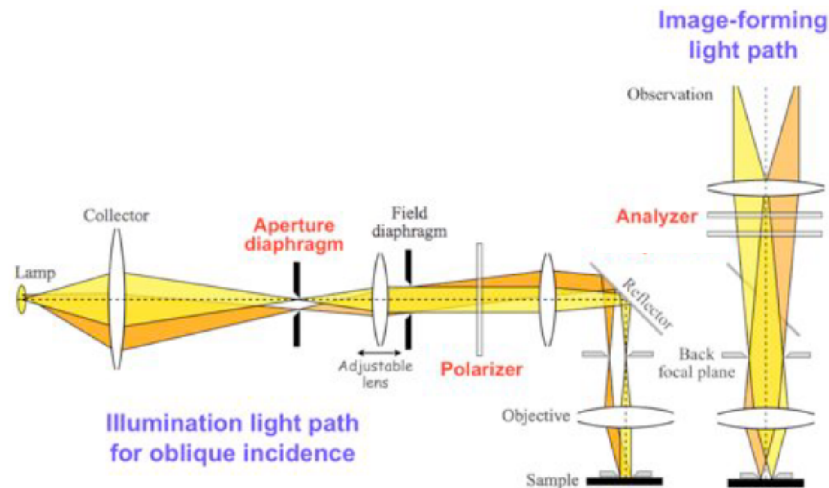
Figure 3.2.: Ray path diagram schematic of wide field magneto-optical Kerr microscope, left - incident light branch, right - reflected light branch, taken from [35].

the magnetization can be manipulated by an external magnetic field. The background image (reference) is usually set as a saturated state. It is then subtracted from a live image containing a particular domain configuration. The ever-present noise in the image can be partially removed by averaging, whereas contrast can afterward be improved by digital contrast enhancement. Better contrast can also be achieved using interference layers.

Measuring the magnetization loops in such a microscope is also possible. The loop is obtained when the average signal of a selected region is plotted as a function of the applied magnetic field.

The LED lamp used is a uniquely developed Kerr-LED lamp consisting of 8 white LEDs. The light is then guided via optical fibers, whereas the ends are arranged in a cross way. An advantage of this configuration is that it allows activating individual LEDs, adjusting the light incidence geometry, and therefore choosing between different Kerr sensitivities (longitudinal, transversal, and polar), indicated in the Figure 3.1. Because of such arrangement of the LEDs, the transversal sensitivity is not actually gained using the transversal- but the longitudinal Kerr effect.

In a basic configuration, the selected LEDs are steadily activated, providing the desired Kerr sensitivity. This mode allows:

(a) longitudinal sensitivity with superimposed polar sensitivity,

(b) transversal sensitivity with superimposed polar sensitivity,

(c) pure polar sensitivity.

The superimposed polar sensitivities are present because the dependence on the polar magnetization component cannot be removed in this mode.

Another configuration is the standard configuration in which the LEDs are run in a pulsed mode, providing:

(d) pure longitudinal sensitivity,

(e) pure transverse sensitivity,

(f) simultaneous longitudinal and transversal sensitivities with superimposed polar sensitivity.

3.3. Quantitative magnetic domain analysis

Usually, we are interested in magnetic thin films or microstructures, which means that the magnetization lies in the plane of the sample, in most cases. When measuring single in-plane sensitivity (i.e., longitudinal or transversal), we get information only about one magnetization component. To map both in-plane magnetization components, we would have to either rotate the sample precisely or adjust the polarizer together with the analyzer. Another possibility is the (f) mode discussed in the previous section, providing simultaneous measurement of both sensitivities by combining experiments at different angles of incidence, which is by far the most convenient.

The most direct principle of determining the whole magnetization function is comparing both images of desired domain configuration (longitudinal and transversal sensitivity) with images of known magnetization states - the saturation states [36].

Our model assumes that the intensity measured by both sensitivities is linear in individual magnetization components and includes a direct component. Furthermore, we assume magnetization being normalized, hence depends only on the radial angle Φ as follows,

$$\boldsymbol{M} = (m_x, m_y) = (\cos \Phi, \sin \Phi). \tag{3.8}$$

The longitudinal intensity I_l then can be written:

$$I_l(\Phi) = A_l \cos \Phi + I_{l,0}, \tag{3.9}$$

where A_l is the amplitude that needs to be normalized, and $I_{l,0}$ is the direct component. The quantities A_l and $I_{l,0}$ can be expressed in terms of maximum $I_{l,max}$ and minimum $I_{l,min}$ values of the I_l function as:

$$A_l = \frac{I_{l,max} - I_{l,min}}{2}, I_{l,0} = \frac{I_{l,max} + I_{l,min}}{2}. \tag{3.10}$$

Substituting back and expressing the cosine term leads us to

$$\cos \Phi = \frac{I_l - \frac{I_{l,max} + I_{l,min}}{2}}{\frac{I_{l,max} - I_{l,min}}{2}} = m_x. \tag{3.11}$$

The same can be repeated for a transversal intensity I_t; therefore, we get

$$\sin \Phi = \frac{I_t - \frac{I_{t,max} + I_{t,min}}{2}}{\frac{I_{t,max} - I_{t,min}}{2}} = m_y. \tag{3.12}$$

The measured image consists of a number of pixels, each having an intensity value. Because each pixel contains information from both sensitivities, we can define in-plane magnetization for each pixel.

Finally, because we are interested in the angle between the magnetization and the $x-$axis Φ, we calculate

$$\Phi = \arctan \left(\frac{m_y}{m_x} \right). \tag{3.13}$$

One of the objectives of this work was to develop a platform for calculating the in-plane magnetization vector field. The graphical user interface (GUI) of the platform was developed in MatLab 2016b and is described in Appendix B.

The reason why we need the reference saturation images is to figure out the quantities $I_{l,max}$, $I_{l,min}$, $I_{t,max}$, and $I_{t,min}$. At the same time, the I_l and I_t are sensitivities of the image we want to investigate.

In Figure 3.3 both horizontal and vertical sensitivity images are plotted in rows, reference images are the first two images of both rows. Note, that saturation images in the first column are homogeneous in intensity due to the image subtraction needed for difference image technique. The column on the right shows a magnetic remanence configuration ($\boldsymbol{H}_{ext} = \boldsymbol{0}$), showing a multidomain state. The output image is converted from a grayscale image to a colorized image to highlight the magnetization vectors orientation, accompanied by plotting a vector field, see image 3.3c). The shown image under research is permalloy microstructures.
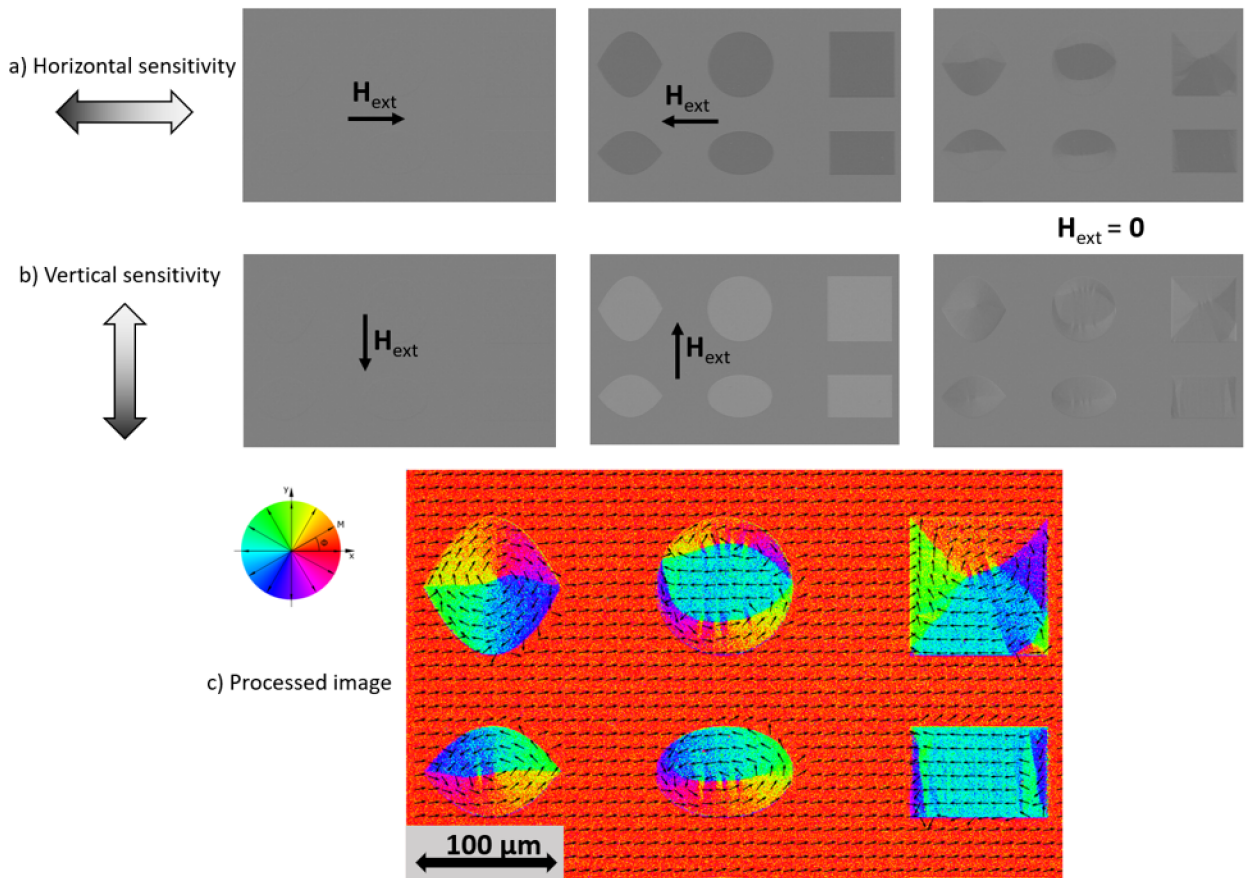

Figure 3.3.: Rows a) and b) show intensity proportional to longitudinal and transversal component of magnetization, respectively. The first two images in each row are reference saturation images needed for calculation of $I_{l,max}$, $I_{l,min}$, $I_{t,max}$, and $I_{t,min}$, last image in corresponding row shows a remanent magnetization state, i.e., state of interest we want to analyze. The resultant image c) is plotted using color-wheel indicating orientation of magnetization together with vector field. The procedure was done on permalloy microstructures.

The platform also allows to post-process the resultant images, which is especially useful when investigating microstructures, it may be beneficial to get rid of the non-magnetic background signal, which is possible in the proposed GUI, as shown in the Figure 3.4. Next example is a permalloy square structure, this time zoomed closer, see Figure 3.5.
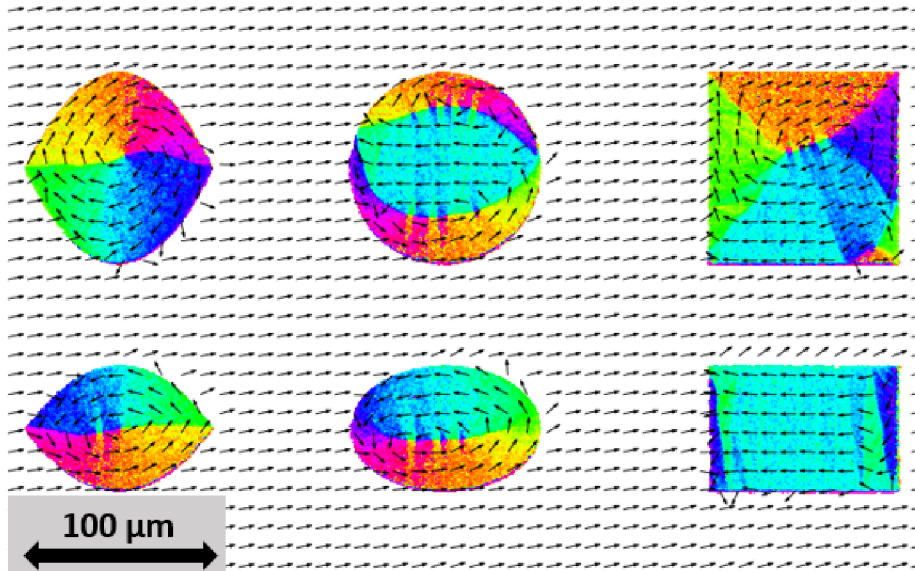

Figure 3.4.: Masked and filtered permalloy structures image using binary mask, which removes undesired background signal.
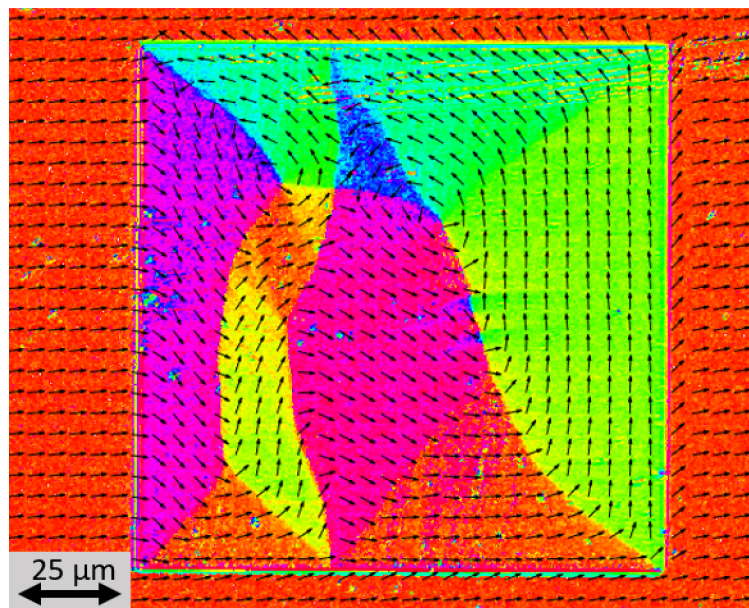

Figure 3.5.: Filtered image of remanent magnetization state of permalloy square structure visualized by proposed computational platform.

3.4. Discussion of measured results

In the permalloy structures images (see Figure 3.4), we can see how different energy terms influence the configuration of magnetic domains. For instance, the structures are large enough to allow magnetization to split into multi-domain states. If the structures were too small, the exchange interaction would tend to hold all the moments lie parallel. An external magnetic field large enough would need to be applied to invert the moments' orientation.

It has to be taken into consideration that permalloy consist of a particular Ni-Fe alloy (with about 80% nickel and 20% iron content) that has nearly zero magnetocrystalline anisotropy, such that no preferential crystalline orientations of magnetization exist. That is why the occurrence of a magnetic vortex state is possible.

Another energy term contributing greatly to the shape of domains is the magnetostatic energy-, or in this case, rather the shape anisotropy term. It appears that the observed system tries its best to avoid magnetization pointing in or out of the structure edge. The magnetization is always parallel to the edges of the structure and creates magnetic flux closure patterns simultaneously.

The next sample under study is a thin film FeRh on a MgO (001) substrate. FeRh thin films were grown epitaxially on MgO (001) substrates using the magnetron sputtering deposition at elevated temperatures and post-growth annealing. The films were grown with assistance of Jon Ander Arregi.

FeRh has a body-centered cubic like (BCC-like) structure, and its lattice parameter corresponds very well to the diagonal lattice parameter of the cubic MgO. This lattice parameter correspondence is the key for epitaxial growth of the FeRh thin film.

In the Figure 3.6, we plotted a multi-domain state of a 40-nm-thick FeRh thin film, the image is filtered. Because of its well-defined crystal structure, the FeRh has two perpendicular easy axes, i.e., the FeRh has the so-called biaxial anisotropy. These easy axes (defined along the in--plane FeRh [100] and [010] direction) correspond to the diagonal orientations in Figure 3.6. We can see that the anisotropy constant of FeRh is relatively large since all moments lie along the diagonal easy axes after demagnetizing the sample using an oscillatory field. Similarly, a raw FeRh thin film image is plotted in Figure 3.7.
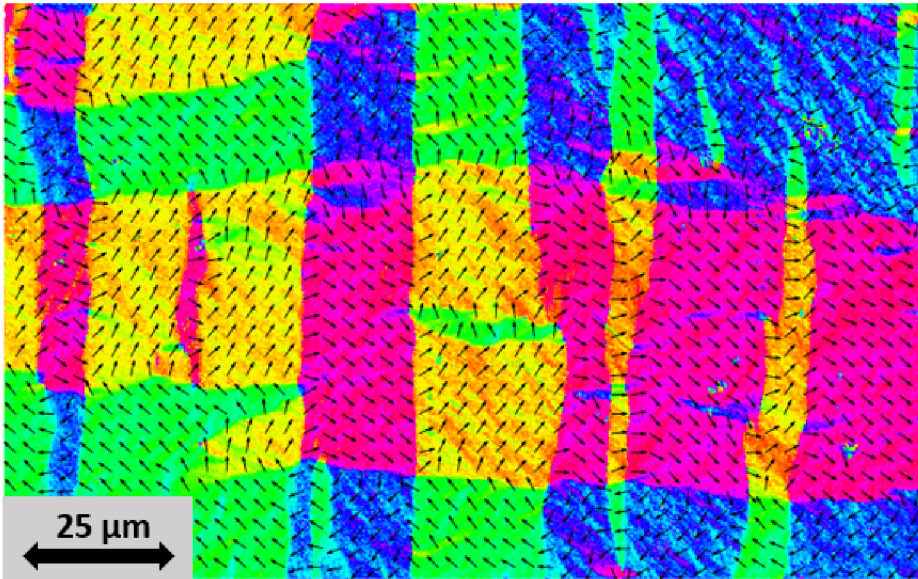
Figure 3.6.: Visualization of remanent magnetization state of FeRh thin film, where the effect of biaxial anisotropy is dominant. Noise extraction was performed using a median filter.
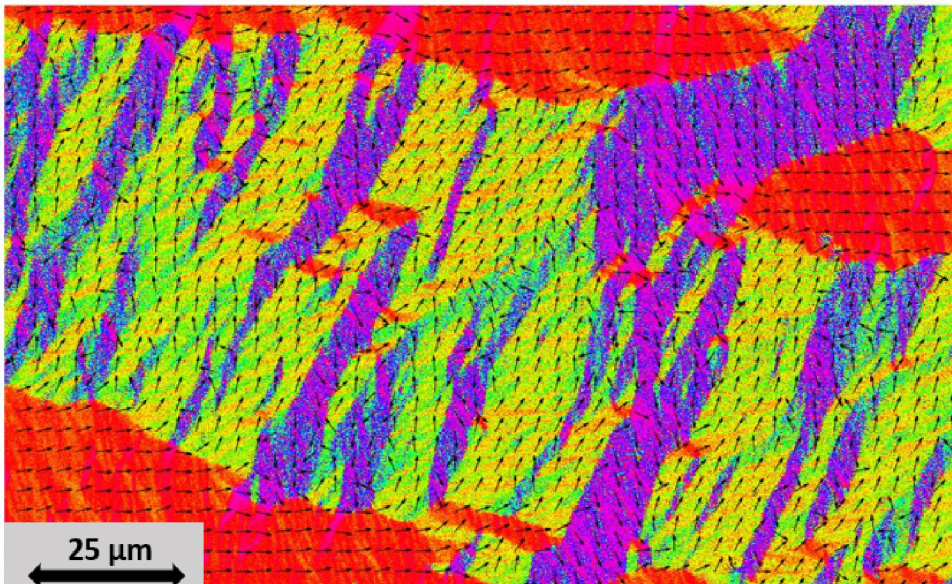

Figure 3.7.: Raw image of a different FeRh remanent magnetization state. No noise extraction techniques were used in this case.

4. Voigt effect observation of magnetic domains

Motivated by the renovated interest in antiferromagnets [12], there are still a lot of properties and phenomena to discover in these materials. In order to understand their behavior better, we need to be able to visualize their magnetic structure. The absence of total magnetization in the antiferromagnet makes its observation using conventional magnetometry difficult. Therefore, the Kerr effects cannot generally be used for antiferromagnetic materials. On the other hand, the Voigt effect is sensitive merely to spin-axis (or to magnetization axis) orientation, with a visual contrast between two orthogonal spin-axis orientations. Because of this, the Voigt effect is a great candidate for magneto-optical observation of antiferromagnetic domain configurations, which was already shown by observing NiO (001) thin film [10].

4.1. Voigt effect description and measurement principle

First-order magneto-optical effects (Kerr and Faraday effect) typically induce primary rotation of polarization plane, including a variation of ellipticity. Thus, we can say that in terms of the reflectivity matrix in Equation (2.22), these effects influence the off-diagonal elements r_{sp}, r_{ps} and r_{pp} of the matrix. In contrast, quadratic magneto-optical effect impact light propagation differently along two perpendicular orientations. We can interpret this like the linear effects may be thought of as "circular magnetic birefringence," and quadratic effect as a magnetically induced linear birefringence [30].

In order to meet a condition for the Voigt effect, we need to come with linearly polarized light at normal incidence. As the light reaches the medium, it decomposes into two eigenmodes, each influenced by a different index of refraction $n_\perp$ and $n_\parallel$ corresponding to the parallel and perpendicular components with respect to the magnetization axis, respectively. After reflection, the two components compose back, but the plane of polarization is rotated because different indices of refraction caused different phase retardation. The rotation is proportional to M^2, and the sense of rotation depends on the relative orientation of the spin-axis and plane of polarization. Furthermore, the reflected light usually contains an ellipticity.

Therefore, upon a geometry in which the incident polarization plane is parallel or perpendicular to the magnetization will not be decomposed, and hence no Voigt rotation appears. However, having the incident light slightly off the magnetization orientation causes some Voigt rotation; the rotation (or the contrast) is maximized when the angle is $45°$.

Basically, the main difference between Kerr and Voigt contrast is its dependence on the magnetization direction: Kerr rotation is direction-sensitive, whereas Voigt rotation is axis-sensitive. This quadratic symmetry of the Voigt effect may be well explained by considering a strain birefringence of material due to magnetostriction. In Kerr effect observation, the best contrast is gained from antiparallel domains. However, for the Voigt effect, the oppositely oriented domains cannot be distinguished. Moreover, the symmetry of a dielectric permittivity tensor in Equation (2.18) results in the maximum domain contrast while, consequently, these domains magnetizations are oriented at $\pm45°$ relatively to initial polarization.

In practice, the reflected light is always elliptical. Because we can detect only linearly polarized light, the combined use of a compensator (phase retarder) and an analyzer is required.

Changing their relative orientation near the extinction condition allows for inversion of the Voigt effect, as well as maximization of the associated Voigt contrast.

4.2. Observation of the Voigt and gradient effect

To obtain sufficient contrast, we use the differential image technique, in which we open the analyzer (or compensator) by a small angle φ, take a background and subtract. Then we set the analyzer (or compensator) to the $-\varphi$ position. Usually, image post-processing methods need to be used to enhance the image quality. These methods include image averaging to improve the signal-to-noise ratio, image shading optimizing an intensity homogeneity of the image, digital contrast adjustment that broadens a histogram of the given image.

When we measure the Voigt effect, we ordinarily encounter some gradient effect contribution. The gradient effect is also a second-order magneto-optical effect, proportional to magnetization change along a certain axis. Due to this, we can detect signal only in areas where magnetization changes. Thus no contrast occurs between domains but rather in the domain walls where the magnetization has to turn quickly; this situation is very well visible in the Figure 2.1. Similar to the Voigt effect, the gradient effect is also sensitive to axes oriented $\pm 45°$ from the incident polarization plane.

We started the Voigt effect measurements with a well-known specimen and ferromagnetic materials so that we could first observe a given domain configurations using linear Kerr effects and thus expect particular results. All the following images were taken at zero external magnetic field.

First, we examined the permalloy structures sample, which we investigated in the previous section; see Figure 3.3. We set the LEDs to fulfill the condition of normal light incidence. The polarizer is set such that the plane of polarization was horizontal. Because of another Voigt effect condition, we could observe domains with magnetization oriented $\pm 45°$ from the polarization plane. To confirm that, we executed this measurement on the selected structure, a rectangle. Due to shape anisotropy energy, a usual multi-domain state is a Landau pattern or similar. The result of the measurement is depicted in the Figure 4.1, where no significant contrast between domains is visible. On the other hand, a strong gradient signal was detected at domain walls, where spatial magnetization gradients concentrate.

In order to visualize the actual domains and not just the domain walls, we need to either rotate the polarizer or the whole sample; since the analyzer can be rotated in a $\pm 10°$ range only, we are not able to conduct the first option, we chose the second. In Figure 4.2a), we present multiple structures. The magnetization state of the oval structures show distinct flux closure states and the rectangular ones show well visible Landau patterns. The inset of the figure defines the spin axis contrast given by the Voigt effect.

Another image was taken with an inversed analyzer position; hence, the contrast is reversed see Figure 4.2b). Again, we can see Landau patterns in the rectangular structures and certain domain configurations in round structures.

Next, we tried to check the resolution limit by imaging smaller structures still using the same objective. The result is plotted in the Figure 4.3a). Except for Landau patterns, magnetic vortices are easily detectable thanks to a characteristic line in the central part of the individual structures originating from the gradient effect. The Figure 4.3b) shows that visualizing even smaller structures (a few microns) is possible.
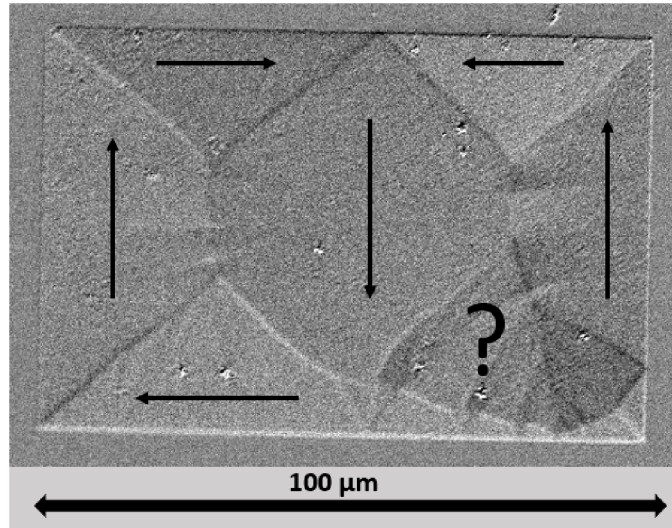
Figure 4.1.: Imaging of a micromagnetic permalloy rectangle via second-order magneto-optical effects illustrating the need for rotation of the sample by $\pm 45°$ in order to see Voigt effect-induced contrast between domains. The image shows prominent gradient effect at domain walls.
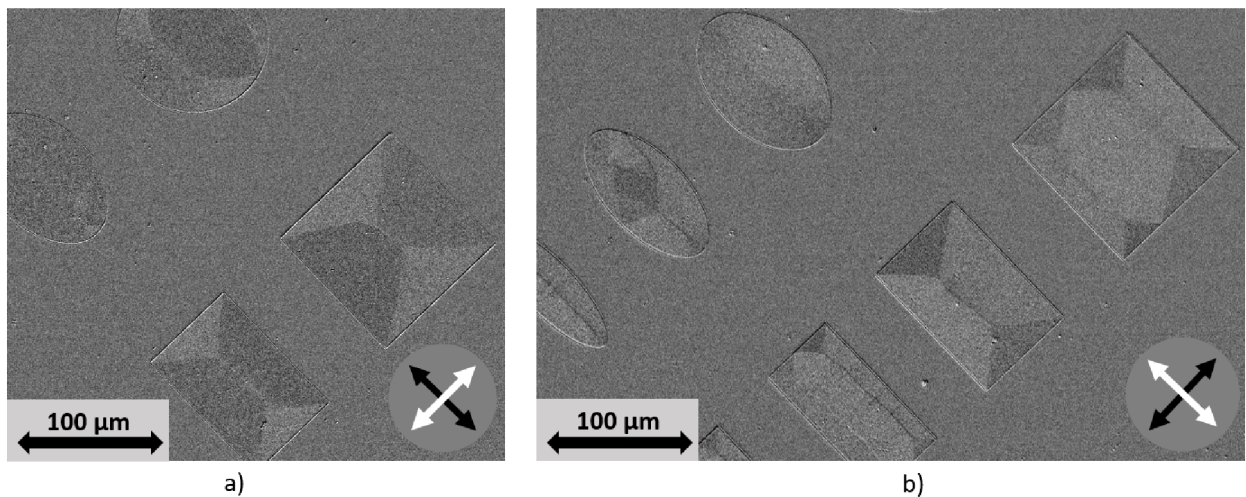

a)   b)

Figure 4.2.: Imaging of remanent magnetization states of permalloy structures using Voigt effect. Rectangular structures are in multi-domain states, creating a Landau patterns. Image a) and b) have opposite analyzer-compensator setting thus showing opposite contrast.

As in the previous section, we also investigated ferromagnetic FeRh thin films. At zero magnetic field (remanent magnetization state), we found out that magnetization likes to lie along the easy axes, which are orthogonal. Upon orienting the easy axes along the diagonal directions in the field of view, magnetic domains in the remanent state correspond well to the Voigt effect sensitivity.

The Figure 4.4 shows a multi-domain state; due to the already mentioned orientation of the easy axes, the measured intensity creates a "checkerboard" pattern.

After rotating the sample by $45°$, the easy axes are also rotated, and so did the domain stripes in the Figure 4.5. Here we can see a significant gradient effect near the domain walls.
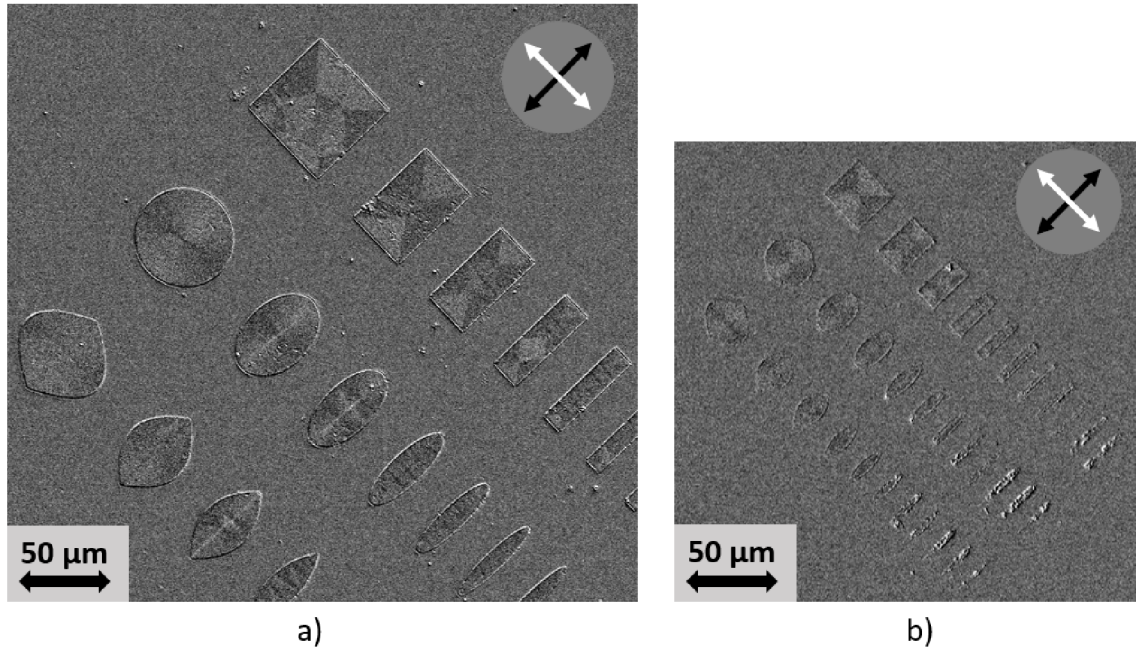
Figure 4.3.: Images a) and b) illustrate that we are able to image magnetic domains using the Voigt effect even in very small permalloy structures.
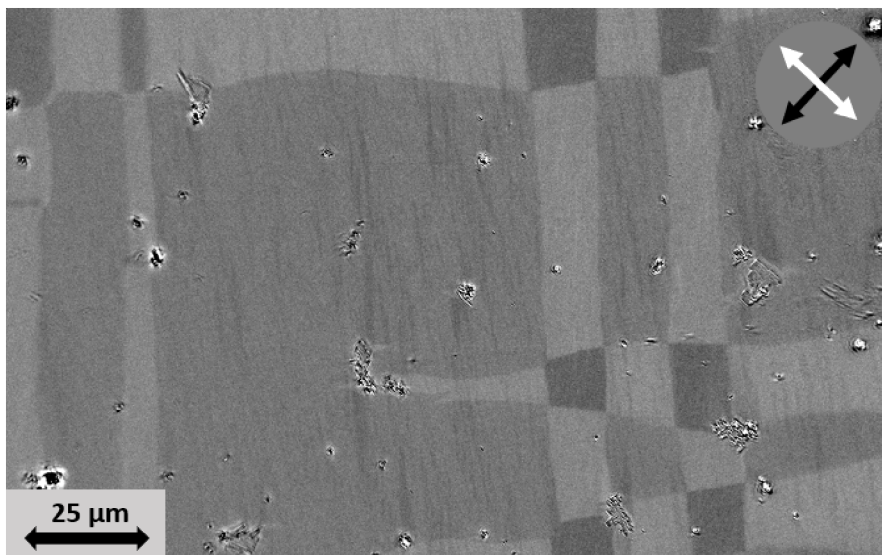

Figure 4.4.: A check-board pattern typical for remanent magnetization state for biaxial anisotropy-dominant FeRh thin film.

4.3. Consecutive Kerr and Voigt imaging

Until now, we were using the second-order effects to visualize magnetization states, but we did not know what the domain configuration looks like precisely. For this reason, we used the quantitative magnetometry platform.

We measured the Voigt image of a chosen domain configuration in the first place. Next, we performed Kerr imaging of the same magnetization state; we had to destroy the state by saturating to gain reference images for the Kerr magnetometry computation. Thanks to this approach, it was possible to plot a magnetization vector field in the Voigt image.
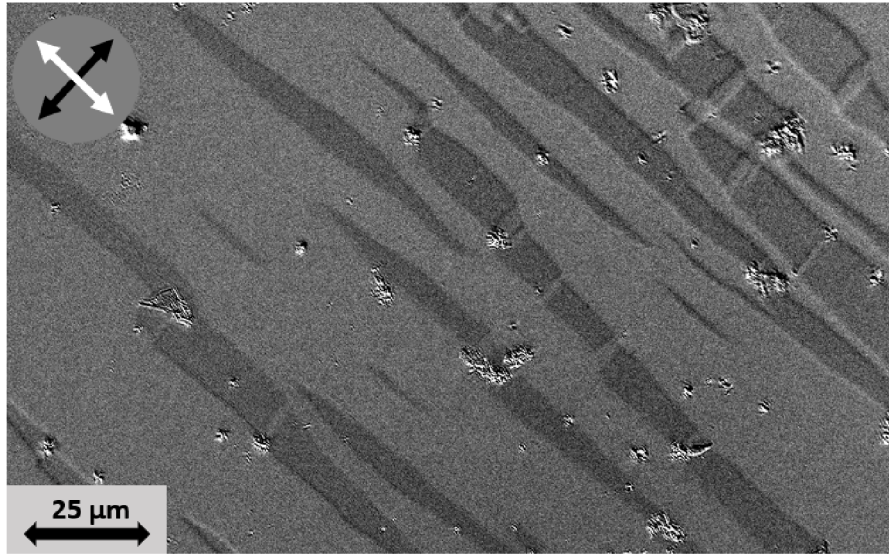
Figure 4.5.: Narrow but long magnetic domains of FeRh thin film, the contrast between domains is visible due to the Voigt effect, in the right upper corner there is a prominent manifestation of the gradient effect.

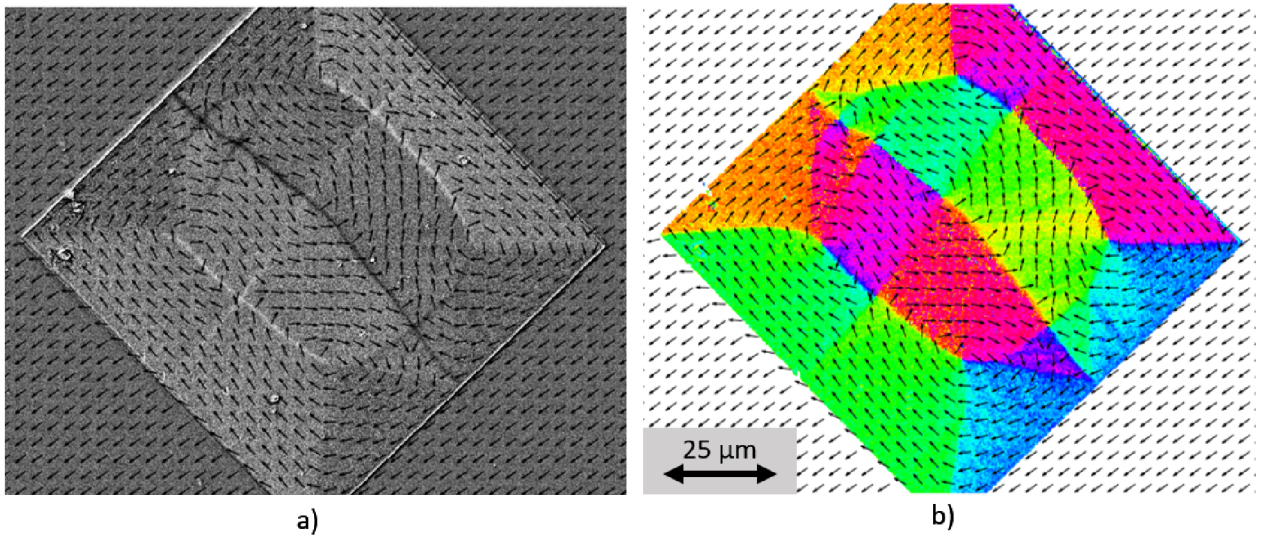a)   b)

Figure 4.6.: Visualization of the same multi-domain configuration of permalloy square via both Voigt imaging and Kerr imaging. The quantitative magnetometry platform displays a colorized magnetization image and vector field with removed background b), the same vector field is than plotted on top of the Voigt image a).

Such procedure was applied on the well-known permalloy structures, this time using an objective with larger amplification. Both images are plotted in the Figure 4.6, in which both Voigt and gradient contrast are significant.

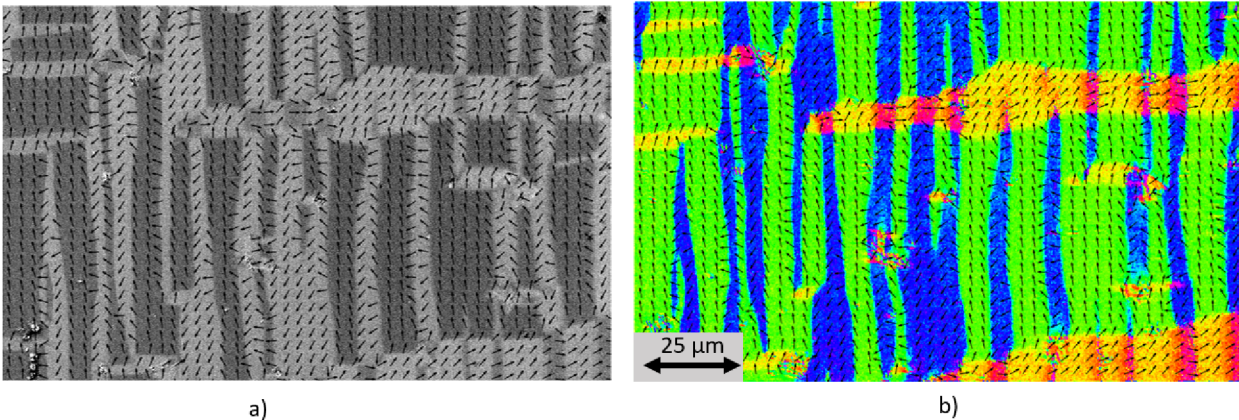The same measurement was done for the ferromagnetic FeRh film; see Figure 4.7.

Figure 4.7.: Kerr b) and Voigt a) imaging performed consecutively to map the magnetization state of FeRh thin film.

4.4. Investigation of antiferromagnetic phase of FeRh using Voigt effect

One of the reasons that make FeRh such an interesting material is that it undergoes a phase transition from anti- to ferromagnetic phase upon heating and vice versa upon cooling. The transition is gradual, and if we measure the dependence of the magnetization on the temperature, we find out that it has a hysteresis-like character.

For temperature-dependent measurements, we mount the sample on a Peltier heating stage. A difference between the two phases is visible by ordinary reflection of the light - no magneto--optics needed, it is because they have different reflection coefficients.

We start at room temperature (the whole film is antiferromagnetic), then heat the sample slowly until the ferromagnetic phase starts appearing, see Figure 4.8a). In this case, the antiferromagnetic phase is bright, and the ferromagnetic phase dark. After heating the sample, even more, the whole film becomes ferromagnetic. Without applying any external magnetic field, we measured the Voigt effect (Figure 4.8b)) and again observed the "check-board-like" pattern, but the domains were much smaller, typically 3 µm, compared to those in figures 3.6 and 4.7, which are usually elongated along one dimension and narrow in the perpendicular one, or form the "check-boards" of characteristic size ≈ 10 µm. Applying an external magnetic field destroys this state, and it is not possible to retrieve the state and form such small domains unless we repeat the cooling and heating process.

Cooling down the sample caused nucleation of the antiferromagnetic phase (bright), as depicted in Figure 4.9a). We did not proceed with the cooling but tried to measure the Voigt effect, see Figure 4.9b), where we see that the antiferromagnetic phase shows contrast only on its edges. This indicates that what we see is a gradient effect when the magnetization is transitioning from one phase to the other. The larger antiferromagnetic region in the left upper corner does not show any hint of the Voigt effect-induced contrast.

The same we see when we let the sample cool down to room temperature, at which the entire film is antiferromagnetic. Measuring the Voigt effect at this point does not provide any domain visualization.

However, we repeated the Voigt effect measurements during heating or cooling with a different sample on which there was a much thicker layer of the FeRh.

We measured the optical reflectivity of the mentioned sample, depicted in the Figure 4.10, both during heating and cooling. From here, we see that antiferromagnetic phase transitions

last near defects when heating and vice versa; nucleates there first during cooling. Also, both phases grow in preferential directions - image diagonals which correspond to the main axes of the FeRh crystal structure, which are the easy axes.

An image gained by reflectivity is plotted in the Figure 4.11a), where again, the darker regions are ferromagnetic while the bright background is antiferromagnetic. When we measured the Voigt effect, see Figure 4.11b), we found that we can get a certain domain picture. In the end, we were able to visualize the ferromagnetic domains, but it is challenging to separate the Voigt- and the gradient effect contributions.

We did the same while cooling, investigating the antiferromagnetic phase, which is plotted in Figure 4.12a) and its Voigt imaging 4.12b), where we managed to see some contrast. Figure 4.12b) proved that it was possible to visualize antiferromagnet using second-order magneto--optical effects.
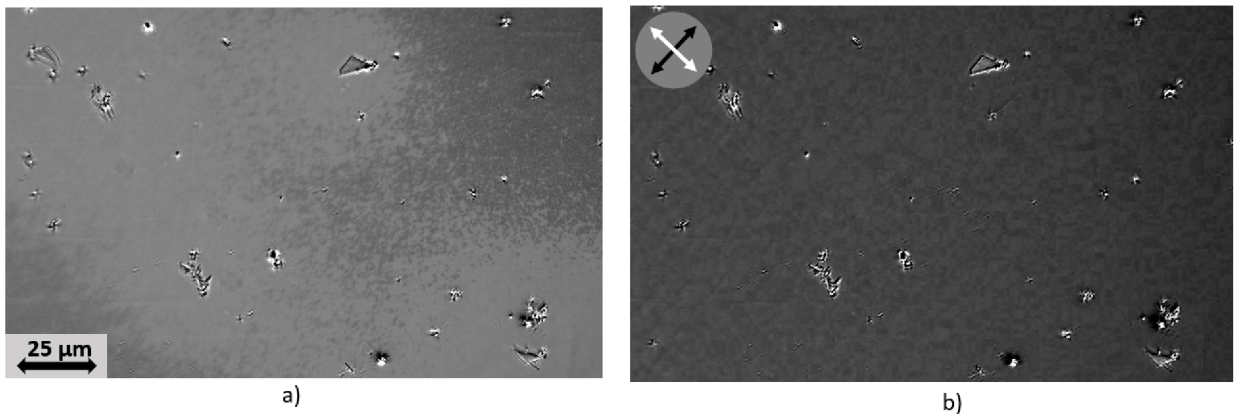

a)   b)

Figure 4.8.: a) Observation of coexistence of ferro- (dark) and antiferromagnetic (bright) phase of FeRh. The image is obtained via regular light reflection, the contrast between the two phases appears due to different reflection indices. Image b) shows a Voigt imaging of fully ferromagnetic FeRh thin film.
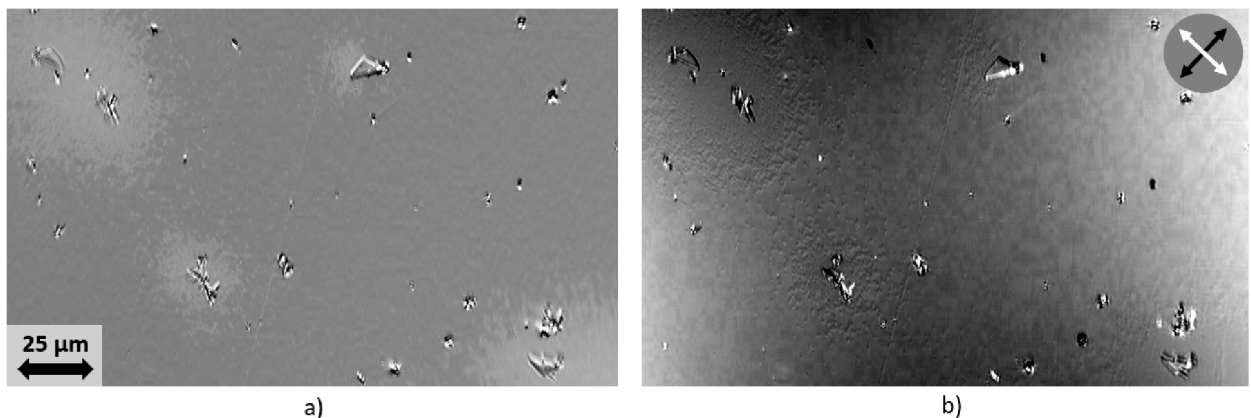

a)   b)

Figure 4.9.: Image a) was gained by light reflectivity technique performed on FeRh during cooling, the antiferromagnetic phase (bright) is growing in the ferromagnetic matrix (dark). The Voigt effect measurement was done upon the same state b), we can see a typical contrast in the ferromagnetic matrix but no contrast in the antiferromagnetic regions.
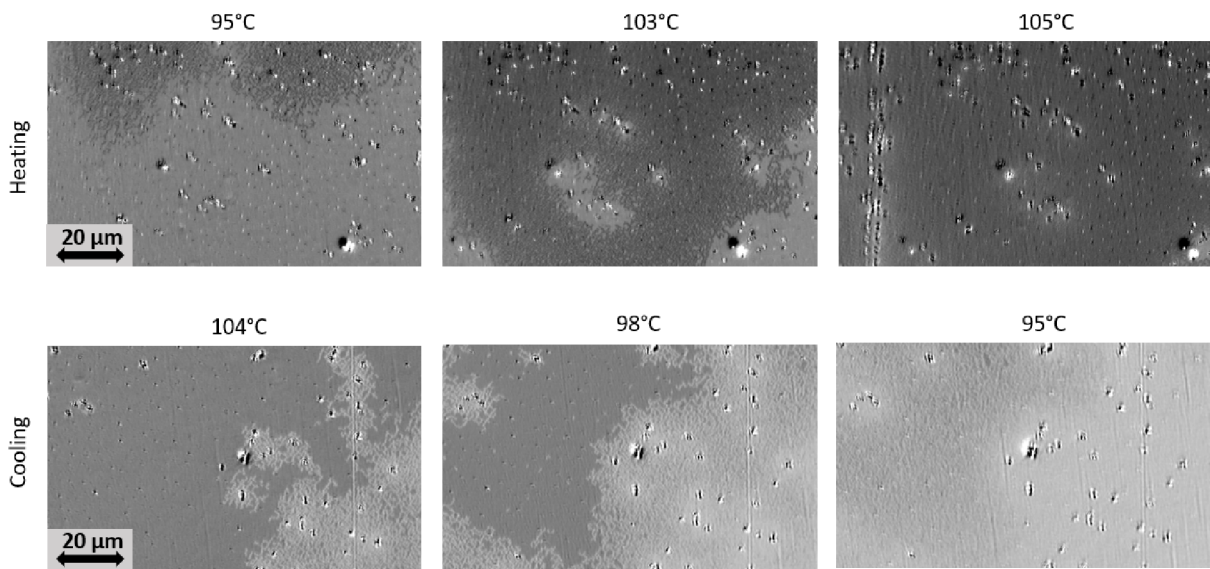
Figure 4.10.: Series of images illustrating nucleation and growth of ferromagnetic and anti-ferromagnetic phase upon heating and cooling, respectively.
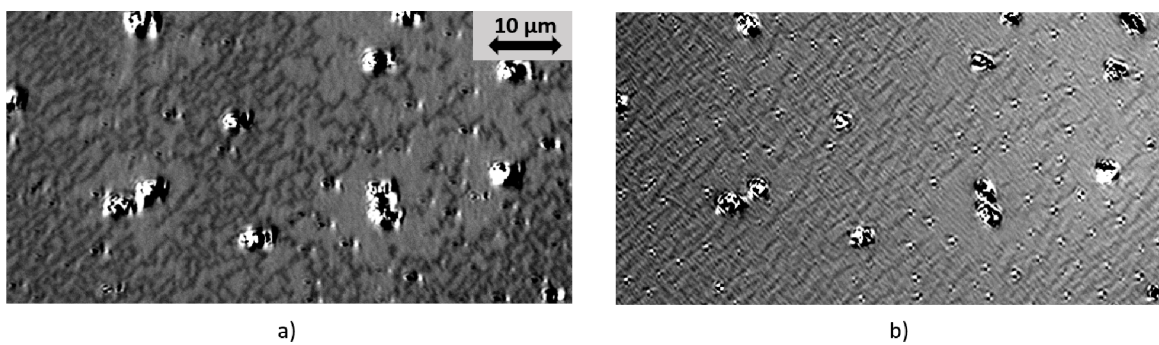

Figure 4.11.: Zoomed view of ferromagnetic phase (dark) of FeRh growing in the antiferro-magnetic matrix (bright) - a) optical refleticity image, b) Voigt imaging.
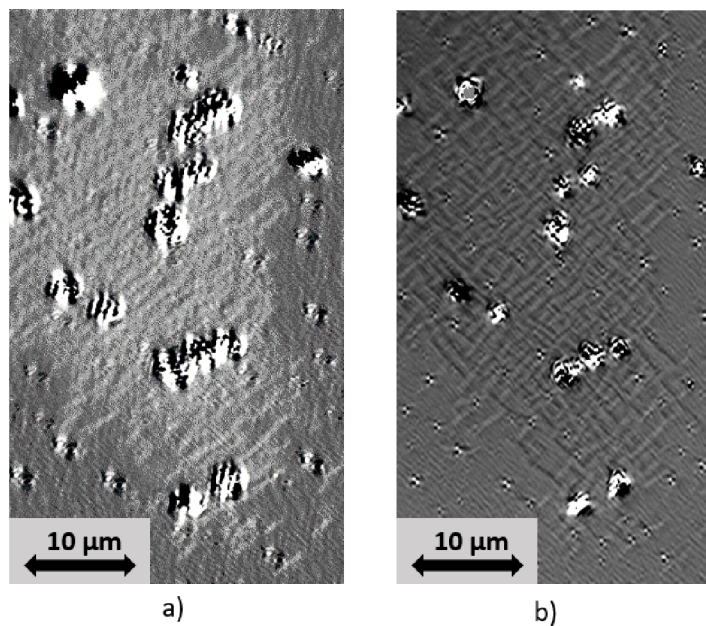
Figure 4.12.: a) Image gained via optical reflectivity technique of antiferromagnetic phase (bright) growing in the ferromagnetic phase (dark). b) Imaging using Voigt- and gradient effects shows the possibility to visualize the antiferromagnetic phase.

Conclusion

In the thesis presented, we pay our attention to the magnetic domain microstructure of the nanoscale magnetic systems with a focus on the visualization of magnetization states.

Initially, the mathematical background that is important for the description of magnetic fields and magnetization in typical magnetic materials is introduced; this chapter also summarizes elementary magnetic interactions leading to various energy terms, as well as their effect on the domain structure. A phenomenological explanation of ferromagnetic hysteresis and magnetization processes is provided.

In the following chapter, we pay our attention to describing the interaction of light with magnetic matter via electromagnetic field theory, i.e., magneto-optics. Here, the Jones formalism is described, a useful mathematical tool for the computation of polarization state changes as light interacts with a sample or various optical components. Special focus is put on the magneto-optical Kerr effect, as well as its macroscopic and microscopic origin.

The experimental results are summarized in two chapters. In the first chapter of the experimental part, we present the experimental analysis path of the polarized light to achieve the separation of Kerr-induced contrast produced by each magnetization component. Next, a strategy is proposed for the computation of the in-plane magnetization vector from Kerr images measured with horizontal and vertical magnetization sensitivity. A graphical user interface designed in the MatLab 2016b environment does the calculation; the developed platform makes the magnetization computation in an automated way using reference images for calibration. The resultant magnetization map is then visualized using both colormap and vector field representations. It also allows for several image processing and noise filtering techniques to improve the output image. The visualization platform is tested on various permalloy microstructures and on FeRh thin film.

The second experimental part is centred on imaging magnetic specimens using second-order magneto-optical effects such as the Voigt and gradient effect. The measurements are again conducted upon the well-known permalloy microstructures as well as the FeRh thin film. Additionally, temperature-dependent reflection contrast imaging is performed to visualize the coexistence of ferromagnetic and antiferromagnetic phases in FeRh. Furthermore, the magnetic state of the regions in each phases is investigated utilizing second-order magneto-optical effects.

REFERENCES

[1] WELLER, D. and MOSER, A.: Thermal effect limits in ultrahigh-density magnetic recording, IEEE Transactions on Magnetics 35, 4423-4439 (1999). ISSN 1941-0069.

[2] NATTERER, F., et al.: Reading and writing single-atom magnets. Nature 543, 226–228 (2017). PMID 28277519.

[3] WOLF, S. A., et al.: Spintronics: a spin-based electronics vision for the future, Science 294, 1488-1495 (2001). ISSN 1095-9203.

[4] CHAPPERT, C., FERT, A. and VAN DAU, F.N.: The Emergence of Spin Electronics in Data Storage. Nature Materials 6, 813-823 (2007). PMID 17972936.

[5] LANGEVIN, P.: Magnétisme et theorie des électrons (Magnetism and the theory of electrons). Ann. Chim. Phys. 5, 70–127 (1905). ISSN 0368-3893.

[6] WEISS, P.: L'hypothése du champ moléculaire et la propriété ferromagnétique (The hypothesis of the molecular field and the property of ferromagnetism). J. de Phys. Rad. 6, 661–690 (1907). doi: 10.1051/jphystap:019070060066100.

[7] HEISENBERG, W.: Zur Theorie des Ferromagnetismus (On the theory of ferromagnetism). Z. Phys. 49, 619–636 (1928). doi: doi.org/10.1007/BF01328601.

[8] KITTEL, C.: Theory of the Structure of Ferromagnetic Domains in Films and Small Particles, Phys. Rev. 70, 965 (1946). doi: doi.org/10.1103/PhysRev.70.965.

[9] BITTER, F.: Experiments on the nature of ferromagnetism. Phys. Rev. 41, 507–515 (1932). doi: doi.org/10.1103/PhysRev.41.507.

[10] XU, J., et al.: Imaging antiferromagnetic domains in nickel oxide thin films by optical birefringence effect. Physical Review B 100, 134413 (2019). doi: doi.org/10.1103/PhysRevB.100.134413.

[11] WADLEY, P. et al. Electrical Switching of an Antiferromagnet. Science 351, 587–590 (2016). ISSN 0036-8075, 1095-9203.

[12] MARTÍ, X., FINA, I. and JUNGWIRTH, T.: Prospect for Antiferromagnetic Spintronics, IEEE Trans. Magn., 51, 2900104 (2015). doi: 10.1109/TMAG.2014.2358939.

[13] BADER, S.: Colloquium: Opportunities in Nanomagnetism. Rev. Mod. Phys. 78, 1-15 (2006). doi: doi.org/10.1103/RevModPhys.78.1.

[14] BLUNDELL, S.: Magnetism in Condensed Matter. Oxford University Press (2001). ISBN 9780198505914.

[15] SPALDIN, N. A.: Magnetic materials: fundamentals and applications. Cambridge University press (2010). ISBN 9780511781599.

[16] HUBERT, A., SCHÄFER, R.: Magnetic Domains: The Analysis of Magnetic Microstructures. Springer-Verlag (1998). ISBN 9783540641087.

[17] TANNER, B. K.: Antiferromagnetic domains. Contemp. Phys. 20, 187-210 (1979). doi: 10.1080/00107517908219099.

[18] CHEONG, SW., et al.: Seeing is believing: visualization of antiferromagnetic domains. npj Quantum Mater. 5, 3 (2020). doi: doi.org/10.1038/s41535-019-0204-x.

[19] COEY, J. M. D.: Magnetism and Magnetic Materials. Cambridge University Press, (2010). ISBN 978-0-511-67743-4.

[20] AHARONI, A., et al.: Introduction to the Theory of Ferromagnetism. Clarendon Press (2000). ISBN 9780198508090.

[21] FLORIDI, L.: Information: A very short introduction. Oxford University Press (2010). ISBN 9780199551378.

[22] MOSER, A., et al.: Magnetic recording: advancing into the future. J. Phys. D: Appl. Phys. 35, R157 (2002). doi: 10.1088/0022-3727/35/19/201.

[23] PARKIN, S. S. P., HAYASHI, M. and THOMAS, L.: Magnetic domain-wall racetrack memory. Science 320, 190-194 (2008). doi: doi.org/10.1126/science.1145799.

[24] KANG, W., et al.: Skyrmion-Electronics: An Overview and Outlook. Proc. IEEE 104, 2040-2061 (2016). doi: 10.1109/JPROC.2016.2591578.

[25] HEINZE, S., et al.: Spontaneous atomic-scale magnetic skyrmion lattice in two dimensions. Nat. Phys. 7, 713-718 (2011). doi: doi.org/10.1038/nphys2045.

[26] FERT, A., CROS, V. and SAMPAIO, J.: Skyrmions on the track. Nat. Nanotechnol. 8, 152-156 (2013). doi: doi.org/10.1038/nnano.2013.29.

[27] FREISER, M. J.: A Survey of Magneto-Optic Effects. IEEE Trans. Magne, 4, 152-161 (1968). ISSN: 1941-0069.

[28] ARREGI, J. A., RIEGO, P. and BERGER, A.: What is the longitudinal magneto-optical Kerr effect? J. Phys. D: Appl. Phys. 50, 03LT01 (2017). doi: 10.1088/1361-6463/aa4ea6.

[29] QIU, Z. Q. and BADER, S. D.: Surface Magneto-Optic Kerr Effect. Rev. Sci. Instrum. 71, 1243–1255 (2000). ISSN 0034-6748, 1089-7623.

[30] KUCH, W., et al.: Magnetic microscopy of layered structures. Springer (2015). ISBN 978-3-662-44532-7.

[31] VISNOVSKY, S.: Optics in Magnetic Multilayers and Nanostructures. CRC Press (2006). ISBN 9781420019193.

[32] YOU, C.Y. and SHIN, S.C.: Generalized Analytic Formulae for Magneto-Optical Kerr Effects. J. Appl. Phys. 84, 541–546 (1998). ISSN 0021-8979, 1089-7550.

[33] BRUNO, P., SUZUKI, Y. and CHAPPERT, C.: Magneto-optical Kerr effect in a paramagnetic overlayer on a ferromagnetic substrate: A spin-polarized quantum size effect. Phys. Rev. B, 53, 9214 (1996). doi: doi.org/10.1103/PhysRevB.53.9214.

[34] ARGYRES, P. N.: Theory of the Faraday and Kerr Effects in Ferromagnetics. Phys. Rev. 97, 334–345 (1955). doi: doi.org/10.1103/PhysRev.97.334.

[35] evico Magnetics GmbH, Magneto-Optical Kerr Microscope & Magnetometer Technical Specifications (2017).

[36] RAVE, W., SCHÄFER, R. and HUBERT, A.: Quantitative observation of magnetic domains with the magneto-optical Kerr effect. J. Magn. Magn. Mater 65, 7-14 (1987). doi: doi.org/10.1016/0304-8853(87)90304-0.

List of abbreviations

HDD   hard disk drive

MOKE   magneto-optical Kerr effect

RCP   right-circularly polarized light

LCP   left-circularly polarized light

LED   light-emitting diode

GUI   graphical user interface

BCC   body-centered cubic

A. Light polarization and optical components in the Jones formalism

We recover the general definition of the Jones vector to represent polarized light as

$$J = \begin{pmatrix} E_x \\ E_y \end{pmatrix} = \begin{pmatrix} E_{0x}\, e^{i\phi x} \\ E_{0y}\, e^{i\phi y} \end{pmatrix}. \tag{A.1}$$

On the following, we may indicate the Jones representations of a set of most common polarization states using this notation. For instance, linearly polarized light with a slope α can be represented as [30]

$$J_\alpha = \begin{pmatrix} \cos\alpha \\ \sin\alpha \end{pmatrix}, \tag{A.2}$$

while both types of circular polarization are expressed as

$$J_{RCP} = \frac{1}{\sqrt{2}} \begin{pmatrix} 1 \\ -i \end{pmatrix}, J_{LCP} = \frac{1}{\sqrt{2}} \begin{pmatrix} 1 \\ i \end{pmatrix}. \tag{A.3}$$

On the other hand, the Jones vector for the most the general elliptical polarization state is

$$J_{ell} = \begin{pmatrix} \cos\Omega \\ \sin\Omega e^{i\Delta\phi} \end{pmatrix}, \tag{A.4}$$

where $\Omega = \arctan\left(E_{0y}/E_{0x}\right)$. Furthermore, the individual components of the $\boldsymbol{E}$-vector may be written in the Jones formalism as follows,

$$J_x = \begin{pmatrix} 1 \\ 0 \end{pmatrix}, J_y = \begin{pmatrix} 0 \\ 1 \end{pmatrix}. \tag{A.5}$$

Because the two components are orthogonal, $J_x \cdot J_y^* = 0$, the two vector form a basis and they are therefore suitable for defining all other polarization states, for example, both circular polarizations:

$$J_{RCP} = \frac{1}{\sqrt{2}} \left(J_x - iJ_y\right), J_{LCP} = \frac{1}{\sqrt{2}} \left(J_x + iJ_y\right). \tag{A.6}$$

We might notice that even $J_{RCP} \cdot J_{LCP}^* = 0$ fulfills, which also means that the RCP and LCP polarization states are orthogonal (and orthornomal), and hence can be used to describe all possible polarization states; for instance, linearly polarized light can be expressed as

$$J_x = \frac{1}{\sqrt{2}} \left(J_{RCP} + J_{LCP}\right), J_y = \frac{i}{\sqrt{2}} \left(J_{RCP} - J_{LCP}\right). \tag{A.7}$$

In addition, we describe here the 2×2 Jonex matrix representation of exemplary optical components acting on the polarization state of light. One of the simplest optical elements is a polarizer. The key role of the polarizer is to change the initial polarization state to a specific

pre-defined state. There are different types of polarizers based on different physical principles, such as absorptive, reflective polarizers, etc. In the following, we will focus on absorptive polarizers.

Absorptive polarizers are made of specific materials whose crystal structure shows optical anisotropy [30]. Linear polarization passing through certain axes remains unchanged, while perpendicular polarization is absorbed; such material is called dichroic. The Jones matrix describing a polarizer polarizing (i.e., letting pass) the incident light along the $x-$axis is given by

$$A_{pol} = \begin{pmatrix} 1 & 0 \\ 0 & 0 \end{pmatrix}. \tag{A.8}$$

If we want to polarize the incoming light along a specified angle α_{pol}, we need to apply a rotational matrix and inverse rotational matrix, leading to

$$A_{pol,\alpha} = \begin{pmatrix} \cos\alpha & -\sin\alpha \\ \sin\alpha & \cos\alpha \end{pmatrix} \begin{pmatrix} 1 & 0 \\ 0 & 0 \end{pmatrix} \begin{pmatrix} \cos\alpha & \sin\alpha \\ -\sin\alpha & \cos\alpha \end{pmatrix} = \begin{pmatrix} \cos\alpha^2 & \cos\alpha\sin\alpha \\ \cos\alpha\sin\alpha & \sin\alpha^2 \end{pmatrix}. \tag{A.9}$$

Another optical element of interest in polarization microscopy is a compensator or phase retarder. The compensator is made of a material that is said to be birefringent. Generally, birefringent materials are the ones that have two different indices of refraction. The incoming light is split into two rays in uniaxial materials, called ordinary and extraordinary, which are perpendicularly polarized. Each ray (or polarization state) experiences a different index of refraction as it passes through the material.

The optical axis with a lower index of refraction is called the fast axis, and the other is termed as the slow axis. This principle is used to modify the incoming polarization state. Using a suitable birefringent plate of a certain thickness, we may compensate the path difference between the two perpendicular polarizations, introducing an effective phase shift between the two. We call such a device a compensator.

In wide-field microscopy, the most used compensators are Brace-Köhler compensators because they cause a homogeneous wavelength-dependent phase shift [16]. Depending on the path difference, there are quarter-wave (i.e. $\lambda/4$) and half-wave (i.e. $\lambda/2$) plates. For instance, incoming light polarized along the x-axis, $J_{in} = \begin{pmatrix} 1 \\ 0 \end{pmatrix}$, passes through a quarter-wave plate with the fast axis rotated by 45°, represented by Jones matrix:

$$A_{qwp} = \frac{1}{\sqrt{2}} \begin{pmatrix} 1 & -i \\ -i & 1 \end{pmatrix}. \tag{A.10}$$

The emerging polarization will be

$$J_{out} = A_{qwp} \cdot J_{in} = \frac{1}{\sqrt{2}} \begin{pmatrix} 1 \\ -i \end{pmatrix}, \tag{A.11}$$

which is a right-circular polarization, or RCP. Of course, the quarter-wave plate can be used vice versa, to change the elliptical or circular polarization to (nearly) linearly polarized light.

B. Quantitative magnetometry GUI

In Figure B.1a), we give a view of the quantitative vectorial magnetometry platform environment. The computational procedure starts with loading reference and to-be-processed magnetization state images. The loading is done by clicking the "Browse" buttons and selecting desired images. The next step is to select the region of interest (ROI), where the user can either put in the coordinates of a ROI rectangle manually and click "Manual" button, or select the other option by clicking the "Cursor" button, such that the user than drags and drops the ROI rectangle in the displayed reference image. The selected ROI must be a magnetic region. This is crucial because within this ROI the program acquires the $I_{l,max}$, $I_{l,min}$, $I_{t,max}$, and $I_{t,min}$ calibration intensities. After pushing the "Process" button, the colorized image is displayed together with a vector field, whose density can be adjusted using a discrete knob. Sometimes, the resultant image is too noisy, for this purpose the application offers different noise filters.

In the second panel in Figure B.1b), the platform allows calculating the relative change of saturation magnetization, this might be especially useful when investigating microstructures. The user selects a magnetic area as well as a background area and thanks to the Kerr contrast as a result of the presence of a saturation magnetization, the magnetic and non-magnetic parts of the image are well separated. Next, a threshold value is selected and a binary mask created, then it is possible to remove the background as well as its vector field. The process of masking the background is depicted in Figure B.1c).
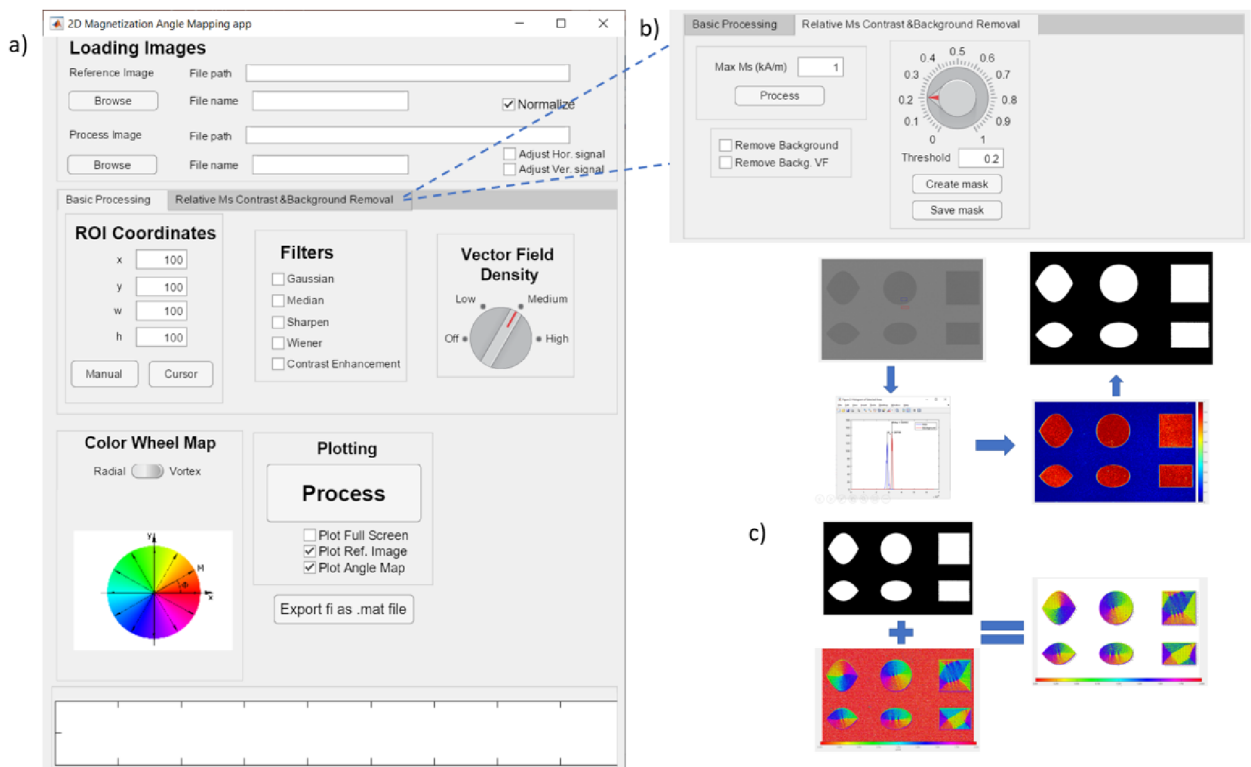

Figure B.1.: a) Graphical user interface of the developed platform - default panel providing basic processing, b) panel calculating relative saturation magnetization change and background removal, c) analysis path of the background removal process.